Photocatalytic zero-length proximity crosslinking reconstructs dynamic protein degradation networks in living cells

Xinyu Zhang[1,2,7], Pengzhi Mao[3,4,7], & Chaohong Bao[2,5,7], Zuye Fang[2], Fenfen Zhang[1,6], Tianyi Deng[1,6], Xi Yang[2], Min Guo[2], Min Zheng[6*], Gang Li[2*]

[1]Shenzhen Medical Academy of Research and Translation, Shenzhen, 518107, China

[2]Institute of Chemical Biology, Shenzhen Bay Laboratory, Shenzhen 518132, China

[3]Key Laboratory of Intelligent Information Processing of Chinese Academy of Sciences (CAS), Institute of Computing Technology, CAS, Beijing, 100190, China

[4]University of Chinese Academy of Sciences, Beijing, 100049, China

[5]State Key Laboratory of Crop Stress Biology for Arid Areas, College of Life Sciences, Northwest A & F University, Yangling 712100 China

[6]Insititute of Infectious Diseases, Shenzhen Bay Laboratory, Shenzhen, 518132, China

[7]These authors contribute equally

*Correspondence: min.zheng@szbl.ac.cn, ligang@szbl.ac.cn

ABSTRACT

Protein interaction networks are dynamically remodeled during signaling and proteostasis, but many transient, low-stoichiometry, or degradation-coupled contacts are lost during affinity purification and difficult to distinguish from proximity-labeling backgrounds. Here, we introduce photocatalytic zero-length proximity crosslinking (PZPC), a genetically encoded, blue-light-

controlled strategy that covalently captures protein-of-interest-containing covalent complexes in living cells. We further develop LinkMasser, a blind-search crosslinking mass spectrometry algorithm that identifies unknown crosslink-associated mass offsets, revealing an oxidative Lys–His zero-length coupling signature underlying PZPC-mediated crosslinking. Using the ubiquitin-independent degradation factor midnolin as a benchmark system, PZPC recovered inducible transcription factors and short-lived regulatory proteins largely missed by conventional AP–MS, leading to the identification of five novel midnolin substrates. We next applied PZPC to 63 human F-box proteins, generating a family-wide proximity atlas of 554 candidate interactors and functionally validating 81 candidate substrates from 257 tested proteins. By coupling this atlas to an antiviral signaling screen, we identified FBXO44 as a positive regulator of the RIG-I–MAVS–IFN pathway and degraded ADAR1, EIF3B, and TUFM as FBXO44-regulated negative modulators of antiviral signaling. These results establish PZPC as a scalable framework for resolving dynamic protein networks and uncovering E3-regulated signaling circuits in living cells.

INTRODUCTION

Protein-protein interactions (PPIs) form dynamic and context-dependent networks that govern nearly every aspect of cellular physiology, including signal transduction, transcriptional regulation, organelle organization, and protein homeostasis[1]. Although the human proteome comprises approximately 20,000 proteins, these components assemble into a far larger and highly plastic interactome that varies across cell types, developmental states, and environmental cues[2]. Many of the most functionally consequential interactions are transient, weak, low-stoichiometry, or conditionally induced, making them difficult to preserve during biochemical isolation and challenging to distinguish from background in living-cell proteomics[3,4]. Methods that can capture

these interactions with high sensitivity, spatial precision, and molecular specificity are therefore essential for understanding how cellular networks are organized and rewired[5,6].

Proximity-based methods have transformed the study of PPIs in native cellular environments. Stoichiometric proximity crosslinking strategies, including those based on genetically encoded unnatural amino acids, can covalently trap interacting proteins with chemically defined linkers[7,8]. However, these approaches often require extensive optimization of insertion sites and typically suffer from low crosslinking efficiency because each installed reactive group acts only once and is susceptible to solvent quenching. Catalytic proximity labeling methods, including APEX[9], BioID/TurboID[10,11], miniSOG-based labeling[12-14], and photocatalytic platforms such as μMap[15], overcome some of these limitations by generating reactive intermediates near a protein of interest (POI)[5,16], thereby amplifying labeling efficiency and enabling detection of weak or transient associations. Yet these methods generally report spatial proximity rather than direct or functionally linked interactions. Because the reactive intermediates are small and diffusible, labeling can extend to nearby but non-interacting proteins, generating backgrounds that complicate interpretation and obscure real interaction events[17,18].

These limitations reveal a central trade-off in proximity-based interactomics: catalytic amplification improves sensitivity, whereas diffusible chemistry compromises spatial confinement. Simply increasing reactivity or shortening intermediate lifetime can reduce diffusion but cannot fully eliminate labeling of neighboring proteins if the reactive species remain freely diffusible. In principle, the effective diffusion distance of a reactive intermediate is governed by both its lifetime and mobility; protein-associated labeling intermediates diffuse much more slowly than small-molecule reactive species and are therefore expected to remain more spatially confined. Inspired by tyrosine–tyrosine crosslinking under oxidative conditions[19], we hypothesized that locally

generated reactive oxygen species (ROS) could first oxidize amino acid side chains, generating protein-associated intermediates that subsequently react with physically associated proteins to form proximity-dependent crosslinked products. Coupling this chemistry to selective enrichment of POI-containing products would further distinguish POI-associated covalent complexes from nonspecific ROS-induced reactions. Such a strategy could retain the sensitivity of catalytic proximity chemistry while improving the molecular specificity needed to resolve dynamic interaction networks in living cells.

Here, we introduce photocatalytic zero-length proximity crosslinking (PZPC), a genetically encoded, blue-light-controlled strategy that combines localized ROS catalysis with POI-restricted enrichment to capture POI-containing covalent complexes in living cells. To define the underlying chemistry, we further develop LinkMasser, a blind-search crosslinking mass spectrometry algorithm that discovers unknown crosslink-associated mass offsets and reveals an oxidative Lys–His zero-length coupling signature. We benchmark PZPC using the ubiquitin-independent degradation factor midnolin, showing that it recovers inducible transcription factors and short-lived regulatory proteins largely missed by conventional AP–MS. We then scale PZPC across 63 human F-box proteins to generate a family-wide interactomics atlas, functionally validate 81 candidate substrates, and identify FBXO44 as a positive regulator of RIG-I-MAVS-IFN signaling through degradation of ADAR1, EIF3B, and TUFM. Together, these studies establish PZPC as a scalable framework for converting proximity chemistry into functionally informative covalent interaction maps, enabling systematic discovery of dynamic protein networks and E3-regulated signaling circuits in living cells.

RESULTS AND DISCUSSION

PZPC enables POI-filtered covalent capture of protein interaction networks. To overcome the trade-off between catalytic labeling efficiency and spatial specificity in proximity-based proteomics, we developed the PZPC platform, a strategy that couples localized ROS generation with POI-restricted enrichment. In PZPC, a genetically encoded photosensitizer is fused to a POI. Upon blue-light irradiation, the photosensitizer catalytically generates ROS in the vicinity of the POI, promoting covalent crosslinking between associated proteins.

A key feature of PZPC is that crosslinking and enrichment are functionally separated. To achieve this, we incorporated an AviTag into the POI fusion construct, allowing site-specific biotinylation by BirA and high-affinity capture of POI-containing species using NeutrAvidin beads (Fig. 1A)[20]. As a result, crosslinked products that contain the POI are selectively retained, whereas ROS-induced reactions that do not involve the POI are removed by stringent SDS- and urea-based washing. This POI-filtering design preserves the sensitivity of catalytic ROS chemistry while reducing background from non-POI-associated oxidation or crosslinking events.

We first optimized the PZPC workflow by evaluating the compatibility of cell lysis conditions with BirA-mediated biotinylation (Fig. S1A–D). We then compared the crosslinking efficiency of three genetically encoded photosensitizers—miniSOG, SOPP2, and SOPP3—using two nuclear proteins, histone H2BC11 and Lamin A, as model POIs. HEK293T cells stably expressing N-terminal photosensitizer and C-terminal AviTag fusion proteins were subjected to blue-light irradiation, affinity enrichment, and immunoblot analysis. For both H2BC11 and Lamin A, light activation produced multiple high-molecular-weight anti-V5-reactive species, consistent with the formation of POI-containing covalent complexes (Fig. 1B, F). Efficient BirA-mediated biotinylation of the POI fusions was also confirmed (Fig. S1J–L), supporting the feasibility of combining photocatalytic crosslinking with AviTag-based enrichment.

We next asked whether PZPC could recover biologically meaningful interaction networks by LC-MS/MS analysis of enriched samples. In the H2BC11 system, SOPP2-based PZPC enriched multiple known or functionally related chromatin-associated proteins, including PPM1G, H2BC18, H2AC25, and H2AZ2 (Fig. 1C). Comparison across photosensitizers revealed distinct recovery profiles. SOPP2 yielded the largest number of candidate interactors and the highest fraction of literature-supported H2BC11-associated proteins compared with miniSOG and SOPP3 (Fig. 1D, E and Fig. S1E-I). We observed similar performance using Lamin A as an independent test case. SOPP2-based PZPC recovered established Lamin A-associated proteins, including LMNB1, LMNB2, EMD, BANF1, and NUP153 (Fig. 1G). Across the three photosensitizers, SOPP2 again produced the strongest interaction recovery and the highest proportion of reference-supported Lamin A interactors (Fig. 1H, I and Fig. S2). Together, these results establish that PZPC can generate POI-filtered covalent interaction maps in living cells and identify SOPP2 as the preferred photosensitizer for subsequent applications.

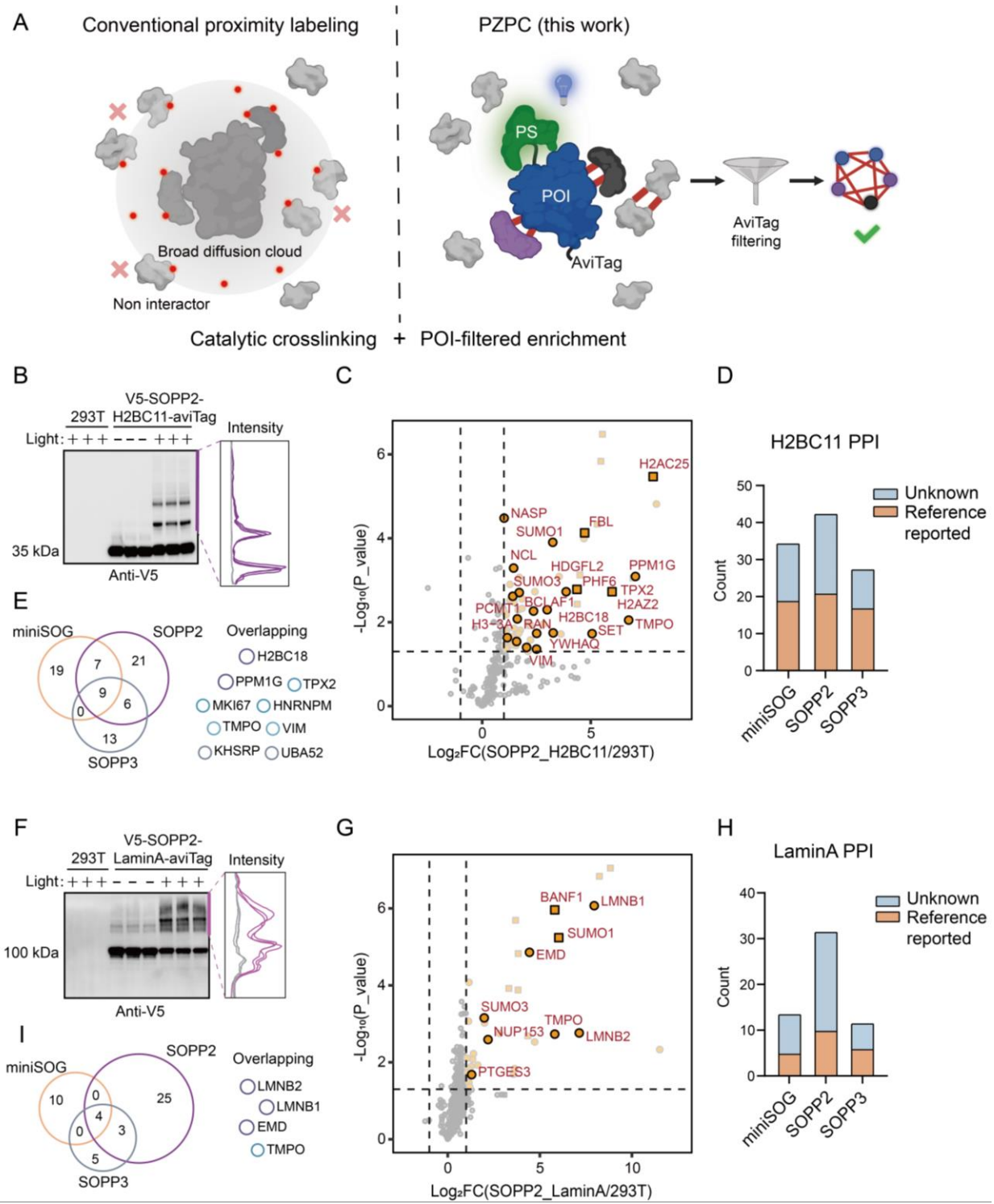

Fig. 1 Development and validation of the PZPC platform for POI-filtered interactome profiling. A) Schematic comparison of conventional proximity labeling and PZPC. Conventional proximity labeling

relies on diffusible reactive intermediates that can label nearby non-interacting proteins. In PZPC, a genetically encoded photosensitizer fused to the POI promotes light-dependent covalent crosslinking, while AviTag-based enrichment selectively retains POI-containing crosslinked products. **B, F**) Anti-V5 immunoblot analysis of V5–SOPP2–H2BC11–AviTag-expressing cells in B or V5–SOPP2–Lamin A–AviTag-expressing cells in F with or without blue-light irradiation. High-molecular-weight species indicate light-dependent formation of POI-containing covalent complexes. Signal intensity profiles are shown on the right. **C, G**) Volcano plots showing proteins enriched from V5–SOPP2–H2BC11–AviTag cells in C or V5–SOPP2–Lamin A–AviTag cells in G relative to parental HEK293T control cells. Statistically enriched proteins are shown as circles, and singletons are shown as squares. Reported or functionally relevant POI-associated proteins are highlighted. **D, H**) Distribution of reference-supported and previously unreported H2BC11-associated proteins in D or Lamin A-associated proteins in H identified using miniSOG-, SOPP2-, or SOPP3-based PZPC. **E, I**) Venn diagrams comparing candidate H2BC11- associated proteins in E or Lamin A-associated proteins in I identified by miniSOG, SOPP2, and SOPP3. Selected overlapping proteins are shown on the right. UBA52 was annotated as a recurrent background protein in the H2BC11 dataset. Experiments were performed at least twice with similar results.

Blind-search crosslinking proteomics identifies a recurrent oxidative Lys–His signature in PZPC. Blue-light irradiation of genetically encoded photosensitizers can generate multiple ROS[14,21], but the species and chemical products responsible for PZPC-mediated covalent capture remained unclear. We first examined the sensitivity of PZPC crosslinking to a panel of ROS scavengers and modulators (Fig. S3A-C). Direct addition of H_2O_2 failed to induce detectable crosslinked species, indicating that bulk peroxide oxidation is insufficient to drive crosslink formation. Sodium azide, a commonly used singlet oxygen quencher, did not suppress crosslinking, and replacement of H_2O with D_2O, which prolongs singlet oxygen lifetime, did not

enhance crosslinking. D-mannitol and vitamin C/ascorbate also had little effect on the crosslinking pattern. In contrast, Trolox markedly reduced crosslink formation across different photosensitizer fusions. Consistently, LC–MS/MS analysis of SOPP2–Lamin A samples showed that Trolox treatment reduced the recovery of known Lamin A-associated proteins, including Lamin B1 and Lamin B2, after normalization to the endogenous biotinylated control protein PCCA (Fig. S3D, E). These results argue against bulk H_2O_2 or freely diffusible singlet oxygen as the sole driver of PZPC crosslinking and instead support a mechanism involving Trolox-sensitive, locally generated radical intermediates.

Defining the chemical nature of PZPC-induced crosslinks is challenging because their mass offsets are not known as a priori. Conventional crosslinking mass spectrometry typically relies on synthetic crosslinkers with predefined spacer masses[22-25]. By contrast, PZPC uses local photooxidation to promote zero-length covalent coupling between protein residues, which requires an unbiased strategy to discover crosslink-associated mass signatures directly from MS/MS data. To address this challenge, we developed LinkMasser, a blind-search crosslinking mass spectrometry algorithm for identifying unknown crosslink-associated mass offsets. LinkMasser first searches tandem mass spectra without precursor-mass constraints to retrieve top-ranked candidate peptide sequences. Candidate α- and β-peptide pairs are then assembled and filtered, and the residual precursor mass offset is calculated by subtracting the combined mass of the two candidate peptides from the observed precursor mass. Recurrent offsets are then clustered using DBSCAN[26] to nominate candidate crosslink-associated masses (Fig. 2A).

We benchmarked LinkMasser using datasets generated with six established chemical crosslinkers, including DSS, DSSO, CDI, ADH, DSBU, and DSBSO. In each case, the dominant mass-offset peaks matched the expected crosslinker-derived modifications, validating the ability

of LinkMasser to recover known crosslink-associated masses without prior specification (Fig. S4A). We then incorporated LinkMasser into the PZPC analysis workflow. Linear peptides were first identified using pFind3[27], and proteins supported by at least two peptide sequences were used to construct a reduced protein database, thereby decreasing the search space for crosslinked peptide identification. LinkMasser was then applied to discover recurrent mass offsets, which were subsequently used as input for pLink3-based assignment of crosslinked peptide pairs (Fig. 2B).

Application of this workflow to SOPP2–H2B samples revealed a prominent recurrent mass offset of approximately +14 Da (Fig. 2C). This mass shift was assigned as H(−2)O(+1), consistent with an oxidative dehydrogenative coupling-associated product[28]. This result indicated that PZPC generates discrete covalent products with a defined mass signature rather than only nonspecific oxidative aggregation. Using the +14-Da offset, pLink3 identified crosslinked peptide pairs in SOPP2–H2B samples. A representative MS/MS spectrum of an intra-protein crosslinked peptide showed fragment ions supporting both peptide chains and localized the crosslink to a Lys–His residue pair within POI-derived peptides (Fig. 2D). Notably, the same +14-Da H2B intra-protein crosslink was also detected in the miniSOG–H2B sample, with the expected single Leu-to-Trp substitution in the β-peptide arising from sequence differences between miniSOG and SOPP2 constructs (Fig. S5A). In addition to intra-protein crosslinks, +14-Da inter-protein crosslinks were detected in the SOPP2–Lamin A proteomic dataset, including a Lamin A–Lamin A crosslink and a Lamin B1/B2–HNRNPU crosslink (Fig. S5B, D). Structural mapping of the Lamin A–Lamin A crosslink placed His-378 and Lys-386 on adjacent Lamin A molecules in close spatial proximity[29], supporting the structural feasibility of the assigned inter-protein crosslink (Fig. S5C).

Based on the recurrent +14-Da mass shift and Lys–His linkage, we propose a working model in which local photooxidation generates an oxidized histidine intermediate that is captured

by a proximal lysine ε-amino group, followed by dehydrogenative coupling to yield a net H(−2)O(+1) mass change (Fig. S4B). This model remains a chemically plausible hypothesis rather than a definitive structural assignment, but it provides a mechanistic framework for the recurrent +14-Da Lys–His crosslinks detected by PZPC. Finally, structural modeling of the SOPP2–H2B intra-protein crosslink using Protenix[30] under a covalent constraint yielded a high-confidence model, further supporting compatibility of the assigned Lys–His linkage with the predicted protein conformation (Fig. 2E). Together, these results establish LinkMasser as an unbiased workflow for decoding PZPC-induced crosslinks, with potential broader utility for elucidating unknown crosslinking chemistries.

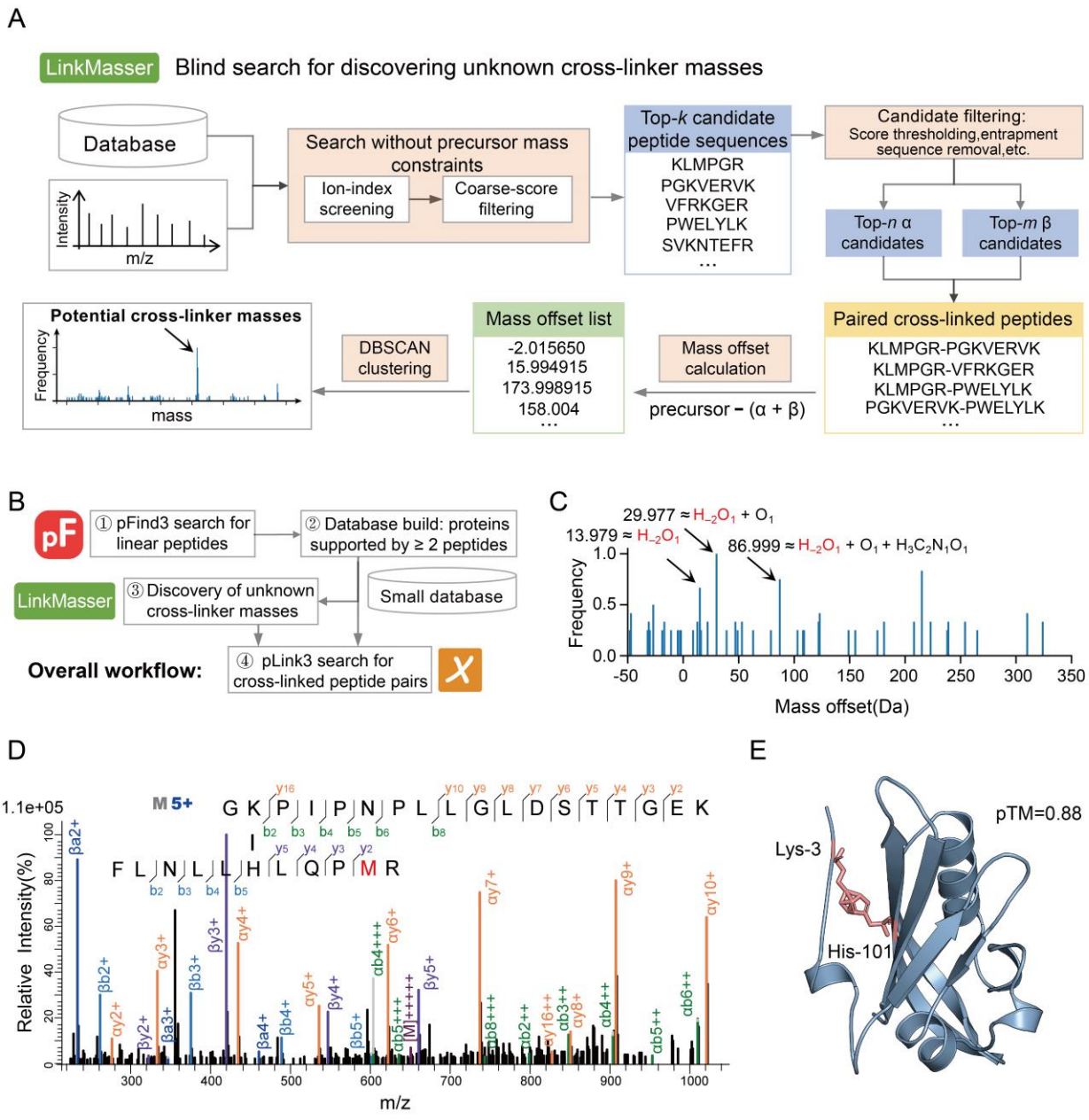

Fig. 2 LinkMasser-enabled blind search identifies a recurrent +14-Da oxidative Lys–His crosslinking signature in PZPC. A) Schematic workflow of LinkMasser, a blind-search algorithm developed to discover unknown crosslink-associated mass offsets from cross-linking mass spectrometry data. MS/MS spectra are searched without predefined precursor-mass constraints to retrieve top-ranked candidate peptide sequences. Candidate peptide pairs are then assembled and filtered, and the residual precursor mass offset is calculated by subtracting the combined mass of the paired peptides from the observed precursor mass.

Recurrent offsets are clustered to nominate candidate crosslink-associated masses. **B**) Overall proteomic data-analysis workflow for PZPC crosslink discovery. Linear peptides are first identified using pFind3, and proteins supported by at least two peptide sequences are used to construct a reduced protein database. LinkMasser is then used to discover recurrent crosslink-associated mass offsets, followed by pLink3-based assignment of crosslinked peptide pairs. **C**) Frequency distribution of candidate mass offsets identified from SOPP2–H2B samples. A prominent recurrent offset of approximately +14 Da was detected and assigned as H(−2)O(+1). Peaks corresponding to methionine oxidation and cysteine iodoacetamide alkylation were also annotated. **D**) Representative MS/MS spectrum of a +14-Da crosslinked peptide pair identified from the SOPP2–H2B sample. Fragment ions supporting both peptide chains are annotated. The localized Lys–His crosslinking residues are highlighted, and oxidized methionine is indicated in red. **E**) AlphaFold3-based structural modeling of the Lys–His crosslink identified in D. The crosslinked residues were modeled onto a truncated protein structure predicted by Protenix under a covalent constraint. The Lys–His linkage is shown as sticks, and the model yielded a pTM score of 0.88.

PZPC captures transient midnolin-associated substrates and regulatory proteins. To benchmark PZPC in a biologically dynamic interaction system, we focused on midnolin (MIDN), a proteasome-associated regulator that promotes ubiquitin-independent protein degradation[31]. Midnolin contains an N-terminal ubiquitin-like domain, two Catch domains, and a C-terminal α-helix, with the Catch domains proposed to recognize substrate degrons and deliver short-lived substrate proteins to the proteasome (Fig. 3A). Because reported MIDN substrates are enriched for immediate-early genes and other rapidly turned-over proteins, this system provides a stringent test of whether PZPC can capture transient substrate-receptor contacts in living cells.

We generated HEK293T cells stably expressing V5-SOPP2-MIDN and first examined light-dependent crosslinking by immunoblotting. Blue-light irradiation induced high-molecular-

weight V5-tagged species, consistent with the formation of MIDN-containing covalent complexes. These signals were enhanced by proteasome inhibition with MG132 and were further increased upon PMA stimulation, conditions expected to stabilize short-lived substrates and induce immediate-early regulatory proteins, respectively (Fig. 3B). Streptavidin-HRP blotting further confirmed the formation of light-dependent biotinylated crosslinked species (Fig. S6A). These results indicate that PZPC captures inducible and degradation-linked MIDN-associated covalent complexes in a condition-dependent manner.

We next performed PZPC-based proteomic profiling of MIDN-containing complexes. Compared with control samples, V5–SOPP2–MIDN treated with PMA and MG132 enriched the known MIDN substrate EGR1 together with a series of immediate-early transcription factors and regulatory proteins, including FOS, JUN, MYC, ATF3, ATF4, CEBPB, YY1, and TRIM33 (Fig. 3C). Under MG132 treatment alone, PZPC recovered a partially overlapping set of MIDN-associated proteins and PMA stimulation further reshaped the MIDN proximity profile, increasing the recovery of inducible transcriptional regulators and revealing PMA-induced MIDN-associated proteins (Fig. S6B-F). Reactome pathway analysis of these PMA-induced candidates highlighted transcriptional and stress-response programs, including ATF4-mediated responses to ER stress, PERK-dependent regulation of gene expression, and nuclear events associated with transcription factor activation (Fig. S6E). Together, these data show that PZPC sensitively reports condition-dependent remodeling of the MIDN-associated protein network.

To determine whether these candidates were incorporated into MIDN-containing crosslinked products rather than simply co-enriched during purification, we performed biotin-mediated enrichment followed by target-specific immunoblotting. Representative candidates, including EGR1, DNAJA1, PPM1G, TRIM28, and JUN, appeared as high-molecular-weight

species after PZPC enrichment, supporting their incorporation into midnolin-containing covalent complexes (Fig. 3D). Thus, the PZPC signal reflects covalent capture of midnolin-associated complexes rather than nonspecific recovery of soluble proteins.

We then asked whether PZPC-enriched candidates were structurally compatible with midnolin recognition. AlphaFold-Multimer predicted multiple possible SOPP2–MIDN-containing complexes, as illustrated by the SOPP2–MIDN–PPM1G model (Fig. 3E). In parallel, AlphaFold3-based modeling suggested that β-strand-like segments from ATF4 and YY1 could be accommodated within the MIDN Catch-domain groove (Fig. 3F). Similar models were obtained for additional candidate substrates, including DACH2, TRIM33, and CEBPB (Fig. S6G). Although these predictions do not define definitive binding modes, they support the possibility that a subset of PZPC-enriched proteins engage MIDN through Catch-domain-mediated degron recognition.

Consistent with this interpretation, immunoblot analysis showed that ATF4, JUN, YY1, TRIM33, and CEBPB exhibited MIDN-dependent abundance changes upon midnolin knockdown or overexpression, supporting their assignment as newly identified candidate substrates (Fig. 3G). By contrast, other PZPC-enriched proteins, including MYC, TNPO1, TNPO2, PPM1G, KAP1/TRIM28, DNAJA1, DNAJA2, ADRM1, and SET, did not show obvious MIDN-dependent abundance changes (Fig. S6H, K). We further examined selected candidates following serum stimulation, a condition known to induce immediate-early proteins. In midnolin-stable cells, CEBPB displayed serum-responsive induction similar to the reported substrate EGR1, whereas IRF2BP2, JUN, and TRIM33 showed more limited serum responsiveness under the tested conditions (Fig. S6I).

Finally, we compared PZPC with previously reported anti-HA IP-MS results for midnolin[31]. Although anti-HA IP-MS recovered more proteins overall, its overlap with PZPC was limited and was dominated by stable proteasome-associated components, including PSMC and PSMD family proteins. By contrast, the PZPC-unique set was preferentially enriched for inducible transcription factors and regulatory proteins, including FOS, FOSB, JUN, EGR1, ATF3, ATF4, CEBPB, YY1, MYC, TRIM33, and DACH2 (Fig. 3H). Many of these proteins are reported substrates or were novelly discovered substrates in this study. Thus, benchmarking against AP–MS shows that PZPC preferentially captures transient, inducible, and degradation-coupled midnolin-associated contacts that are underrepresented in conventional affinity purification. These results establish midnolin as a stringent test case for PZPC and demonstrate the ability of the platform to reveal functionally informative substrate–receptor interaction networks in living cells.

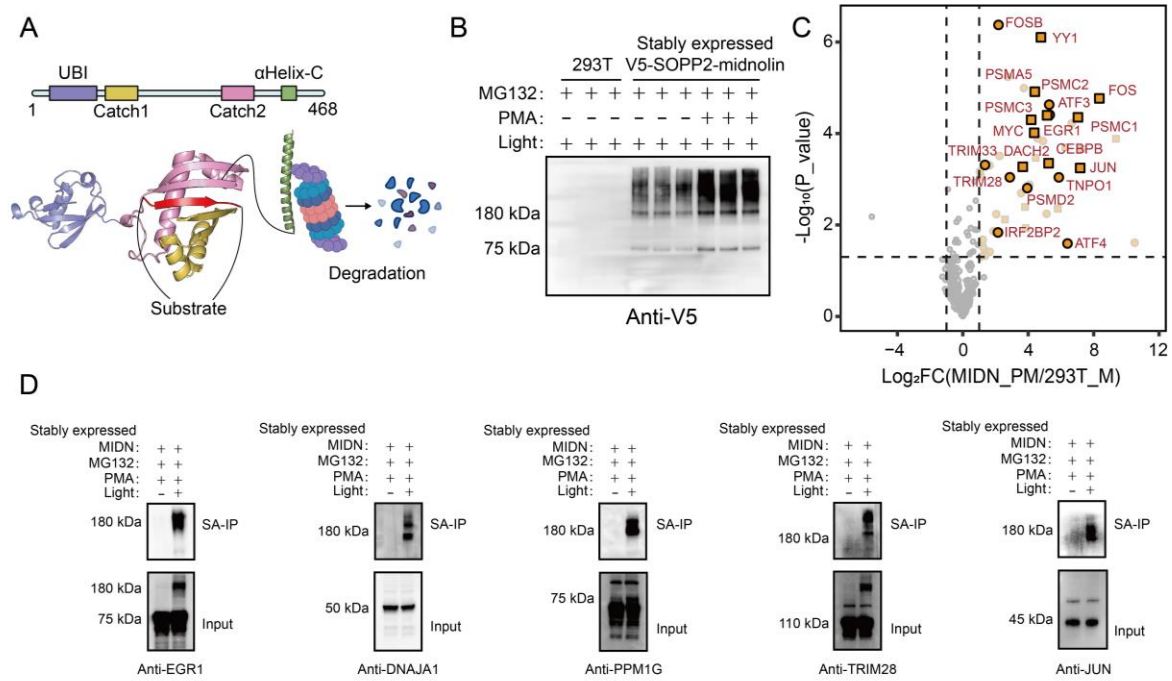

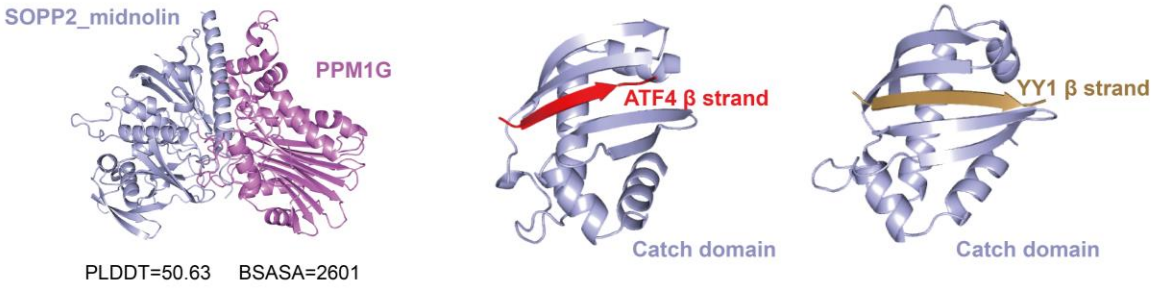

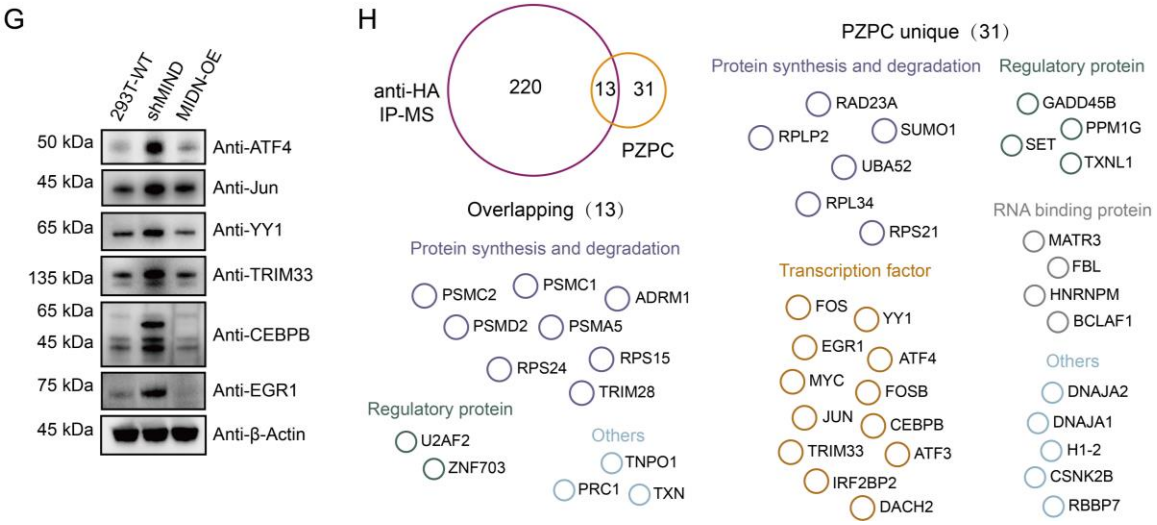

299

Fig. 3 PZPC benchmarking captures transient midnolin-associated substrates and regulatory proteins. A) Schematic of midnolin domain organization and its proposed substrate-recognition model. Midnolin contains an N-terminal ubiquitin-like domain, two Catch domains, and a C-terminal α-helix. The Catch domains recognize substrate degrons and promote ubiquitin-independent proteasomal degradation. **B**) Anti-V5 immunoblot analysis of PZPC-mediated crosslinking in HEK293T cells stably expressing V5–SOPP2–MIDN. Cells were treated with MG132, PMA, and blue light as indicated. High-molecular-weight V5-reactive species indicate light-dependent formation of MIDN-containing covalent complexes. **C**) Volcano plot showing proteins enriched in the V5–SOPP2–MIDN cells treated with PMA and MG132 relative to control HEK293T cells treated with MG132. Statistically enriched proteins are shown as circles, and singletons are shown as squares. The known midnolin substrate EGR1 and representative candidate midnolin-associated proteins are highlighted. **D**) Immunoblot validation of representative midnolin-containing crosslinked products. Biotin-mediated enrichment was performed to isolate SOPP2–MIDN-containing complexes, followed by immunoblotting with antibodies against the indicated candidate proteins. High-molecular-weight bands indicate incorporation of the candidates into midnolin-containing covalent complexes. Input samples are shown below. **E**) Representative AlphaFold-Multimer prediction of the SOPP2–MIDN–PPM1G complex. The model is shown with the indicated predicted local distance difference test (pLDDT) and buried solvent-accessible surface area (BSASA) values. **F**) AlphaFold3-based models of the midnolin Catch domain bound to degron-like β-strand segments from ATF4 or YY1. Predicted substrate β-strands are shown in red for ATF4 and brown for YY1. **G**) Immunoblot analysis of representative candidate midnolin-regulated proteins in HEK293T-WT, shMIDN, and midnolin-overexpressing cells. EGR1 was included as a positive control, together with candidate substrates ATF4, JUN, YY1, TRIM33, and CEBPB. β-Actin was used as a loading control. **H**) Comparison of proteins identified by conventional anti-HA IP–MS and PZPC. The Venn diagram summarizes overlapping and PZPC-unique candidates. Selected proteins are grouped by functional category, including protein synthesis and degradation, regulatory proteins, transcription factors, RNA-binding proteins, and others. Experiments were repeated at least twice with consistent results.

A family-wide F-box proximity atlas reveals modular degradation-associated interaction networks. Having established that PZPC can capture transient midnolin-associated substrate contacts, we next asked whether this strategy could be scaled to systematically map interaction networks for a large family of substrate-recognition proteins. We focused on human F-box proteins, which serve as substrate-recruiting modules in SKP1–CUL1–F-box (SCF) E3 ubiquitin ligase complexes. By engaging diverse substrates through their variable substrate-recognition domains, F-box proteins control protein turnover across many biological pathways (Fig. 4A)[32]. However, systematic characterization of F-box substrate-recognition landscapes remains challenging because many E3–substrate interactions are transient, low-stoichiometry, and coupled to rapid proteasomal degradation. We therefore reasoned that the covalent and proximity-restricted nature of PZPC could provide a powerful strategy to capture these otherwise labile interactions across an entire E3 substrate-receptor family.

We first optimized the PZPC configuration using SKP2/FBXL1 as a model F-box protein[33]. Comparison of fusion orientation and expression strategy showed that transient expression of an N-terminal AviTag–SOPP2–SKP2 fusion produced stronger light-dependent crosslinked signals and more robust proteomic recovery than either a stable cell line or the corresponding C-terminally tagged SOPP2–SKP2–AviTag construct (Fig. S7A–D). The reduced performance of the C-terminal fusion is consistent with potential interference with F-box-associated interaction surfaces or substrate-recognition regions. MG132 treatment was included before blue-light irradiation to stabilize short-lived substrates and associated complexes. Under the optimized condition, SKP2 profiling recovered expected SCF- and proteostasis-associated proteins, including SKP1, UBE2M, RNF126 and PSMD2, supporting the feasibility of PZPC for F-box proximity mapping.

We next extended this strategy to 63 human F-box proteins, covering 33 FBXO, 21 FBXL and 9 FBXW family members (Fig. 4B, Fig S9-21). Representative profiles from the three subfamilies revealed distinct enrichment patterns, as illustrated by FBXO2, FBXW2 and FBXL2 (Fig. 4C). Across the full dataset, PZPC identified 554 unique candidate interactors under stringent enrichment criteria. The global enrichment distribution showed a median log2 fold change of 3.31 (Q1 = 1.587, Q3 = 5.29), indicating a strong signal-to-background ratio across the atlas (Fig. S7E). Candidate interactor numbers varied substantially across the family, ranging from highly connected members such as FBXO2, FBXL18 and FBXW2 to F-box proteins with more selective proximity profiles, with an average of 31 candidate interactors per F-box protein (Fig. S7F). We then assembled a family-wide F-box proximity interaction map, which revealed a highly heterogeneous but structured interaction landscape across the FBXO, FBXL and FBXW subfamilies (Fig. 4D).

Several features emerged from this atlas. First, PZPC robustly recovered canonical SCF-associated components, including SKP1, CUL1 and RBX1, validating the ability of the approach to capture core F-box complex architecture in cells. Second, multiple chaperone and protein quality-control factors, including DNAJA1, HSP90AA1 and HSP90AB1, appeared as recurrent hub-like interactors across many F-box proteins. This pattern suggests that F-box substrate recognition is closely coupled to protein folding, chaperone-assisted substrate loading or quality-control surveillance. Third, in addition to canonical SCF components, CUL4B was unexpectedly enriched with a subset of F-box proteins, together with RBX1. Co-immunoprecipitation validated representative CUL4B-associated F-box proteins, including FBXL2, FBXL6, FBXL6 and FBXL10 (Fig. S8A-D). These results raise the possibility that selected F-box proteins may participate in non-canonical cullin-associated assemblies. Interestingly, we also observed cross-F-

box detection events, with several F-box proteins, including FBXL18, FBXL2 and FBXO39, appearing as prey proteins in other F-box datasets. Together with the recovery of CAND1[34-36], a known regulator of cullin–RING ligase remodeling and F-box exchange, in several F-box profiles. These observations are consistent with the possibility that PZPC captures dynamic exchange or higher-order organization within the broader CRL network.

Beyond core ligase architecture, the atlas revealed broad connections between F-box proteins and major cellular regulatory systems. Multiple cell-cycle and proliferation-associated proteins, including CDK2, PCNA, MCM proteins, TP53, RUVBL1 and other mitotic or replication factors, were enriched in specific F-box profiles. These findings support a broad role for F-box proteins in coordinating cell-cycle progression, DNA replication, chromatin regulation and mitotic control. We also detected cytoskeleton-associated proteins, including FLNA, MAP4, ACTB, DYNLL2, PLS3 and CLTC. Notably, CLTC is a core component of the TACC3–ch-TOG–clathrin complex, which has been implicated in stabilizing kinetochore fibers of the mitotic spindle by forming inter-microtubule bridges[37]. Thus, the F-box proximity atlas links selected F-box proteins not only to CDK-driven cell-cycle regulation but also to cytoskeletal and spindle-associated processes, suggesting a potential coupling between proteolytic regulation and mitotic architecture. In parallel, many F-box proteins were linked to proteasome-associated and ubiquitin-system factors, including PSMD2, PSMC3, RAD23A, RAD23B, ADRM1, UBA1, UBE2M, UBAP2L, SUMO3 and UBQLN2. We also observed recurrent enrichment of non-canonical ubiquitin ligases or ubiquitin-related regulators, such as HUWE1[38], JADE2[39], RNF126, RNF214, TRIM28, STUB1[40], RCHY1[41], MGRN1[42] and RANBP2, suggesting extensive crosstalk between F-box proteins and broader ubiquitin-ligase networks.

A further prominent theme was the connection between F-box proteins and protein quality-control/ER-associated degradation pathways. VCP/p97 and BAG6 were repeatedly detected across multiple F-box datasets, together with ER or secretory-pathway components such as HSP90B1/GRP94, CANX[43,44] and SEC61A1 in selected profiles. These observations suggest that subsets of F-box proteins may be functionally coupled with protein triage, retro-translocation or ER-associated degradation rather than acting solely on classical cytosolic substrates. Representative interactions identified by PZPC, including F-box associations with PHB2, AMOT, PDGFRB and p53, were further validated by co-immunoprecipitation (Fig. S8E-J).

Together, this family-wide analysis establishes PZPC as a scalable strategy for mapping transient E3 substrate-receptor proximity networks in living cells. Rather than producing a simple list of candidate interactors, the F-box atlas reveals a modular and highly heterogeneous degradation-associated interaction landscape, linking individual F-box proteins to canonical SCF assembly, non-canonical cullin-associated complexes, chaperone-assisted quality control, cell-cycle regulation and ERAD[45,46]-related proteostasis pathways. These data provide a resource for discovering F-box substrates and regulatory mechanisms and demonstrate the power of PZPC to systematically resolve transient protein-interaction networks that are difficult to capture by conventional affinity purification.

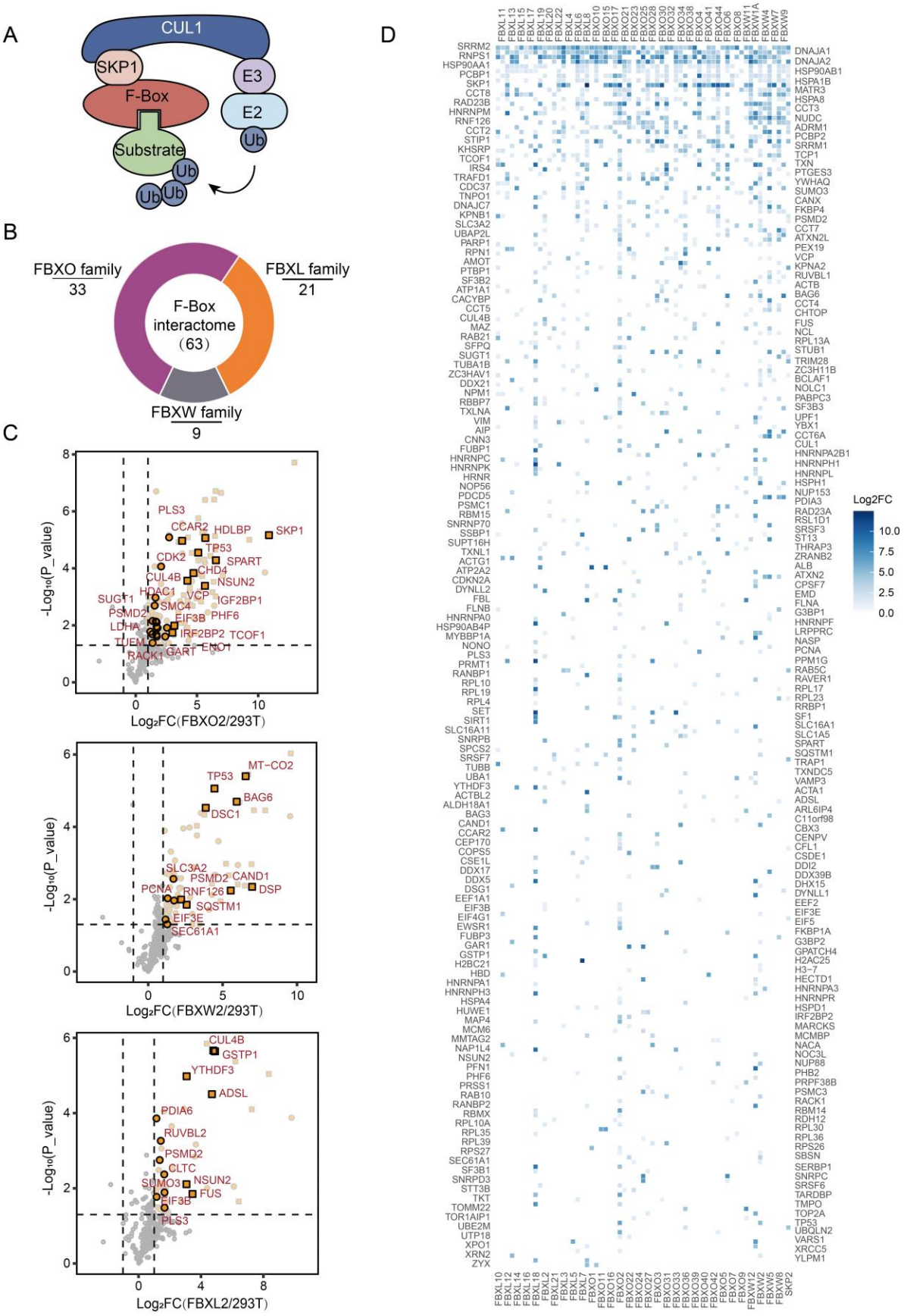

413

Fig. 4 PZPC profiling of the human F-box protein interactome atlas. A) Schematic representation of an SCF-type E3 ubiquitin ligase complex. F-box proteins serve as substrate-recognition modules that are associated with SKP1 and CUL1 to recruit substrates for ubiquitination. **B**) Composition of the F-box proteins profiled in this study. A total of 63 F-box proteins were analyzed, including 33 FBXO, 21 FBXL and 9 FBXW family members. **C**) Representative volcano plots showing PZPC-enriched interactors for one example from each F-box subfamily. Significantly enriched candidate interactors are highlighted and labeled. **D**) Global interaction map of the 63 profiled F-box proteins. Heatmap shows candidate F-box-associated proteins identified by PZPC across the FBXO, FBXL and FBXW families. Color intensity indicates enrichment relative to the control, shown as log2 fold change. UBA52 and PNN were removed as common background proteins.

Functional validation converts the F-box proximity atlas into a candidate substrate network. Having established a family-wide F-box proximity atlas, we next asked whether PZPC-enriched interactors could be further prioritized as functional degradation substrates. Because proximity capture alone cannot distinguish substrates from adaptors, cofactors or stable complex components, we implemented a secondary validation workflow based on perturbation-dependent protein stabilization. PZPC-enriched candidates detected in fewer than three F-box profiles were prioritized to identify relatively selective F-box-associated substrates. In parallel, we searched the F-box interaction database for proteins containing the reported DSGXXS phosphodegron motif[47,48], identifying CTNNB1, TCOF1, SRRM2, RBM15, and URB2 as additional candidate substrates for validation. Each candidate was then examined by immunoblotting after siRNA-mediated depletion of its corresponding F-box protein, with increased protein abundance used as the criterion for F-box-dependent regulation (Fig. 5A).

F-box knockdown was confirmed by RT–qPCR or immunoblotting when suitable antibodies were available (Fig. S30-33). We first used the FBXO34-AMOT pair as a representative example. AMOT was identified as a candidate FBXO34-associated protein by PZPC, and co-immunoprecipitation confirmed the interaction between endogenous AMOT and V5-tagged FBXO34 (Fig. 5B). Depletion of FBXO34 using three independent siRNAs increased AMOT abundance, as well as additional FBXO34-associated candidates including DBN1 and EMD (Fig. 5C). Cycloheximide-chase analysis further showed that AMOT was stabilized upon FBXO34 knockdown, supporting regulation at the level of protein turnover rather than indirect transcriptional induction (Fig. 5D). Conversely, increasing expression of FBXO34 reduced AMOT protein abundance in a dose-dependent manner (Fig. 5E). Together, these orthogonal experiments support AMOT as a candidate FBXO34-regulated substrate.

We then extended this validation strategy across the F-box family. Representative examples included FBXL6-associated candidates TKT, TCOF1, GANAB and SLC7A5; FBXO22-associated candidates NUMA1 and BAG3; and FBXW2-associated candidates SQSTM1, DSC1 and DSP, which showed increased abundance upon depletion of the corresponding F-box protein in at least two siRNA conditions (Fig. 5F–H). Across the full validation set, we tested 257 candidate proteins and identified 81 reproducibly stabilized candidates, corresponding to an overall validation rate of approximately 30% (Fig. S22-29).

The resulting validation map revealed a selective yet modular F-box substrate network (Fig. 5I). Validated candidates spanned all three F-box subfamilies and covered diverse biological processes, including transcriptional regulation, RNA processing, cytoskeletal organization, metabolism, protein quality control and cell-cycle control. Most substrates were stabilized by depletion of only one or a few F-box proteins, arguing against broadly promiscuous regulation and

suggesting substantial substrate selectivity across the family. Conversely, several F-box proteins, including FBXO2, FBXO34, FBXL8, FBXL18, FBXW1A and FBXW2, showed multiple validated substrates, indicating heterogeneous substrate-regulatory capacity among individual F-box proteins. Hierarchical clustering further suggested groups of substrates that may be co-regulated by related or overlapping F-box proteins, pointing to potential degradation modules linked to specific cellular processes. Importantly, this validation scheme provides a functional filter to distinguish candidate degradation targets from non-degradative interactors or condition-dependent associations. Together, these results convert the PZPC-derived F-box proximity atlas into a functional degradation map and establish an integrated proximity-capture/perturbation workflow for scalable discovery of F-box-dependent degradation pathways.

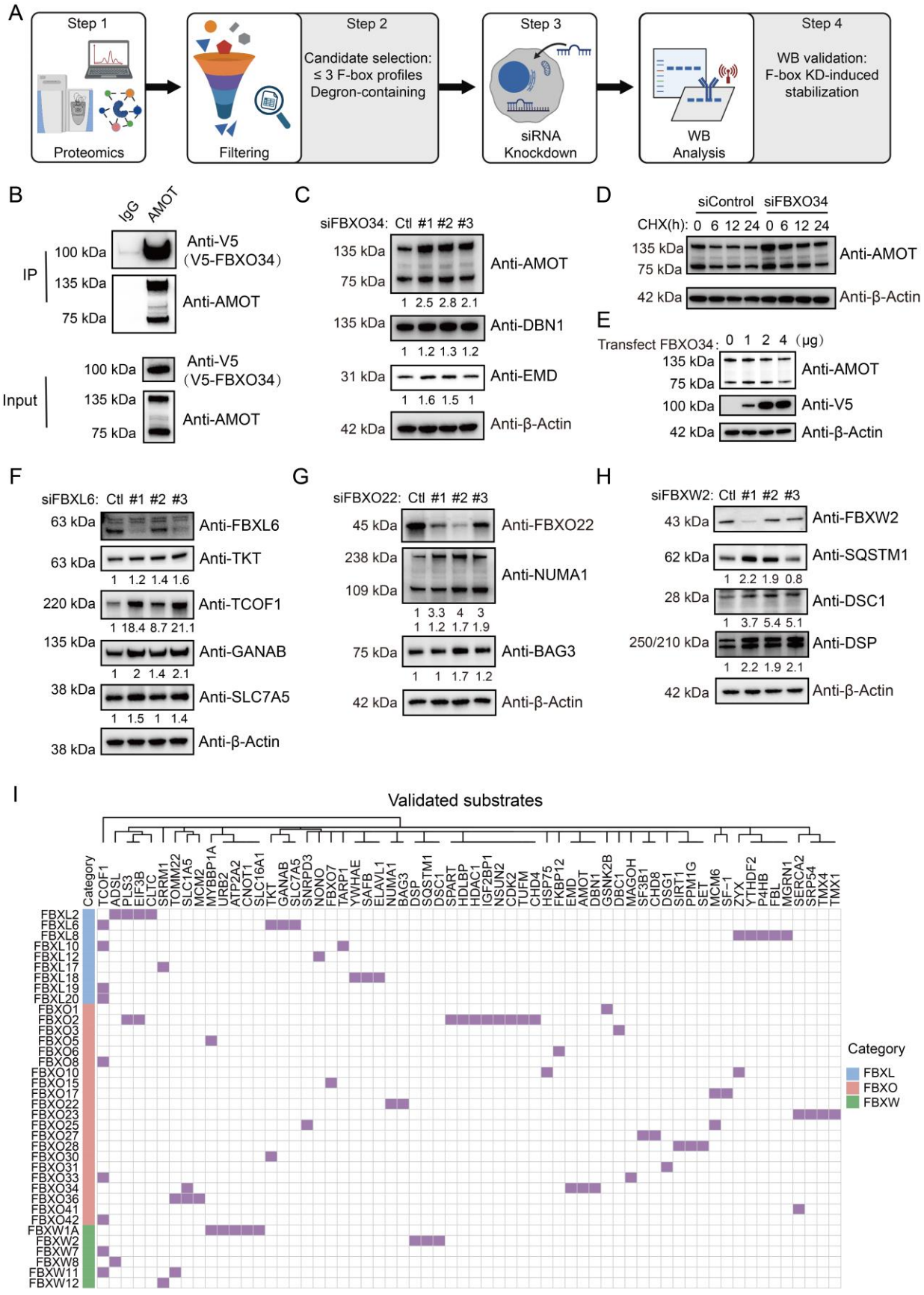

Fig. 5 Functional validation of F-box-associated proteins identifies candidate degradation substrates. **A**) Workflow for systematic validation of candidate F-box substrates. PZPC-enriched candidate interactors detected in fewer than three F-box proximity profiles as well as proteins with reported DSGXXS phosphodegron were prioritized for siRNA-based functional screening. After siRNA-mediated knockdown of the corresponding F-box protein, candidate interactor abundance was measured by immunoblotting to identify proteins stabilized upon F-box depletion. **B**) Co-immunoprecipitation validation of the FBXO34–AMOT interaction. V5-tagged FBXO34 was detected after AMOT immunoprecipitation, with IgG as a negative control. **C**) Immunoblot analysis of representative candidates after FBXO34 knockdown using three independent siRNAs. AMOT, DBN1 and EMD showed increased abundance upon FBXO34 depletion. β-Actin was used as a loading control. **D**) Cycloheximide-chase analysis of AMOT stability in control and FBXO34-depleted cells at the indicated time points. FBXO34 knockdown stabilized AMOT. **E**) Dose-dependent regulation of AMOT by FBXO34. Increasing amounts of FBXO34 plasmid reduced AMOT protein abundance. **F–H**) Representative validation of additional F-box–candidate substrate pairs by siRNA-mediated F-box knockdown and immunoblotting. Candidate substrates showed increased abundance after depletion of the corresponding F-box protein. **I**) Summary heatmap of validated candidate F-box substrates across the family. Purple boxes indicate F-box–substrate pairs supported by immunoblot validation. F-box proteins are grouped by subfamily. All substrate-validation experiments were repeated at least twice with consistent results.

PZPC-guided functional screening reveals an FBXO44-centered antiviral regulatory circuit.

Having established a family-wide proximity atlas of F-box proteins, we next asked whether this resource could uncover pathway-specific functions of individual F-box members. We focused on innate antiviral signaling, a process governed by inducible protein–protein interactions and proteasome-dependent regulation[49,50]. To functionally interrogate the F-box family, we established an ISRE-driven luciferase reporter assay in HEK293T cells, in which individual F-box proteins

were transiently expressed before Sendai virus (SeV) infection and type I interferon-ISGF3 pathway activation was quantified by luciferase activity (Fig. 6A).

This family-wide screen revealed a heterogeneous regulatory landscape, with most F-box proteins showing limited effects on SeV-induced ISRE activity, whereas a small subset reproducibly modulated the antiviral response (Fig. 6B). Among these, FBXO44 emerged as the strongest positive regulator. Because SeV activates RIG-I–MAVS signaling, leading to type-I interferon production, JAK–STAT activation and induction of interferon-stimulated genes (ISGs)[51,52], we further evaluated the effect of FBXO44 at endogenous signaling outputs (Fig. 6C). FBXO44 overexpression markedly increased SeV-induced expression of *IFNB1* and *IFIT1*, as well as *ISG15, Mx1* and *TNFα* (Fig. 6D and Fig. S34B), and enhanced STAT1 phosphorylation, particularly at 9–12 h post infection (Fig. S34A). Conversely, FBXO44 depletion reduced SeV-induced STAT1 activation and attenuated the induction of *IFNB1, IFIT1, ISG15*, *Mx1* and *IL6* (Fig. 6E, F and Fig. S34C). Together, these data establish FBXO44 as a previously undercharacterized positive regulator of the RIG-I–MAVS–IFN signaling axis.

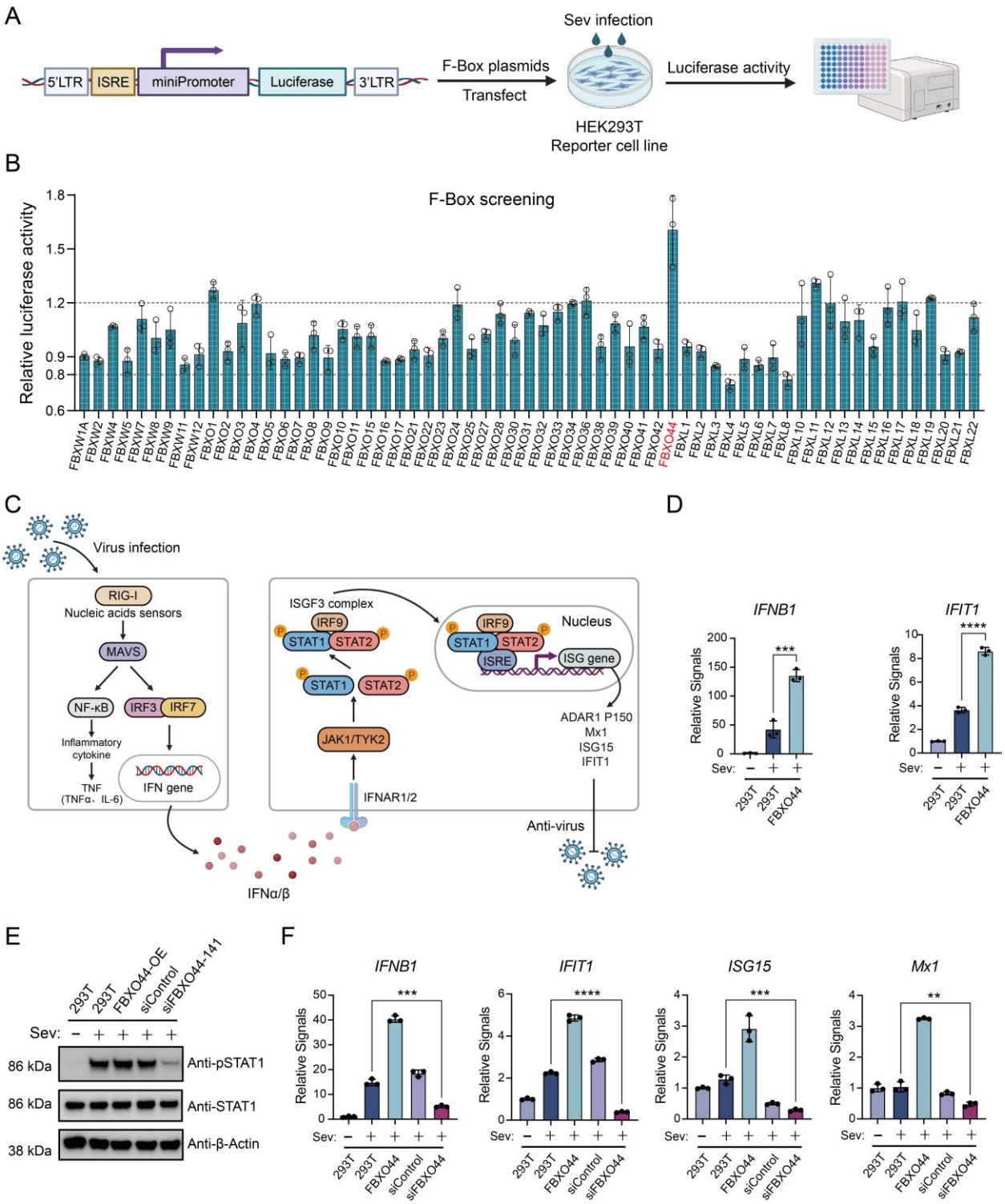

Fig. 6 Functional screening identifies FBXO44 as a positive regulator of RIG-I–MAVS signaling. A) Workflow of the ISRE-driven luciferase reporter screen. HEK293T ISRE–luciferase reporter cells were transiently transfected with individual F-box expression plasmids, infected with Sendai virus (SeV), and

assayed for luciferase activity. **B**) Family-wide F-box screen using the ISRE reporter assay after SeV infection. Relative luciferase activity for each F-box construct was normalized to the empty vector control. Dotted lines indicate 80% and 120% of the baseline reporter response. Points denote independent replicates; bars indicate mean ± s.d. **C**) Schematic of the RIG-I–MAVS–IFN signaling pathway and ISRE-dependent transcriptional output. Viral RNA sensing activates RIG-I–MAVS signaling, leading to IRF-dependent IFN production, JAK–STAT activation and induction of interferon-stimulated genes (ISGs). **D**) Gain-of-function validation of FBXO44. qPCR analysis of *IFNB1* and *IFIT1* expression following SeV infection in control and FBXO44-overexpressing cells. **E**) Immunoblot analysis of STAT1 phosphorylation following SeV infection in control, FBXO44-overexpressing and FBXO44-depleted cells. Total STAT1 and β-actin were used as controls. **F**) Loss-of-function validation of FBXO44. qPCR analysis of *IFNB1, IFIT1, ISG15* and *Mx1* expression following SeV infection in cells treated with control or FBXO44-targeting siRNAs. Statistical significance was determined by two-tailed unpaired Student's t test; $^{**}P < 0.01$, $^{***}P < 0.001$, $^{****}P < 0.0001$. Experiments were repeated at least twice with similar results.

We next used PZPC to define the FBXO44-associated protein network under viral infection conditions. HEK293T cells expressing AviTag–SOPP2–FBXO44 showed robust light-dependent formation of high-molecular-weight FBXO44-containing species after SeV infection, as detected by anti-V5 immunoblotting. Streptavidin–HRP blotting further confirmed the generation of biotinylated crosslinked products, indicating efficient capture of FBXO44-proximal complexes in infected cells (Fig. 7A). Quantitative proteomic profiling identified a focused FBXO44 proximity network enriched under SeV stimulation (Fig. 7B). In addition to canonical ubiquitin–proteasome and SCF-associated components, including SKP1, PSMC1, PSMD2 and RNF126, this network contained proteins linked to innate immunity, RNA metabolism and viral responses, such as ADAR1, EIF3B, TUFM, DDX17, ZC3HAV1, TRIM28, PUM2 and TTC4[53]. Reactome analysis

549 reinforced this functional connection, revealing enrichment for proteasome-mediated protein
550 catabolism, regulation of protein ubiquitination, innate immune response, defense response to
551 virus, positive regulation of RIG-I signaling and viral gene expression-related processes (Fig. 7C).
552 Thus, PZPC placed FBXO44 at the interface between ubiquitin-dependent proteostasis and
553 antiviral signaling.

554 We validated representative FBXO44-associated proteins by co-immunoprecipitation.
555 EIF3B, TUFM and ADAR1 reproducibly co-precipitated with V5-tagged FBXO44, supporting
556 their association under the tested conditions (Fig. 7D). We then used protein abundance changes
557 after FBXO44 depletion as a functional filter to distinguish candidate regulatory substrates from
558 non-degradative interactors. Among selected FBXO44-proximal proteins, ADAR1 p150 isoform,
559 TUFM and EIF3B increased upon FBXO44 knockdown, whereas TTC4, PUM2, TRIM28,
560 ZC3HAV1 and DDX17 showed limited or no consistent stabilization under the same conditions
561 (Fig. 7E and Fig. S34D). These results nominate ADAR1 p150, TUFM and EIF3B as candidate
562 FBXO44-regulated proteins within the antiviral proximity network.

563 Finally, we asked whether these FBXO44-regulated candidates influence antiviral
564 signaling output. Individual depletion of TUFM, EIF3B or ADAR1 enhanced SeV-induced
565 STAT1 phosphorylation (Fig. 7F), which is in line with the reported roles of TUFM and ADAR1
566 in interferon pathways[54,55]. Consistently, knockdown of each candidate increased expression of
567 antiviral genes, including *IFNB1, IFIT1, ISG15* and *Mx1* (Fig. 7G and Fig. S34E). These data
568 indicate that TUFM, EIF3B and ADAR1 act as negative modulators of the antiviral response in
569 this cellular context. Together with the FBXO44 gain- and loss-of-function results, these findings
570 support a model in which FBXO44 promotes RIG-I–MAVS–IFN signaling by restraining
571 inhibitory proteins within the antiviral network (Fig. 7H).

Collectively, this section reveals an FBXO44-centered antiviral regulatory circuit. The family-wide ISRE screen first nominated FBXO44 as a positive regulator of SeV-induced antiviral signaling. PZPC then resolved an infection-associated FBXO44 proximity network enriched for ubiquitin–proteasome and innate immune regulators. Finally, perturbation of FBXO44-proximal candidates identified ADAR1 p150, TUFM and EIF3B as negative modulators whose abundance is controlled, directly or indirectly, by FBXO44. Thus, PZPC does not simply catalog proximity interactions, but enables functional reconstruction of E3-regulated signaling circuits in living cells.

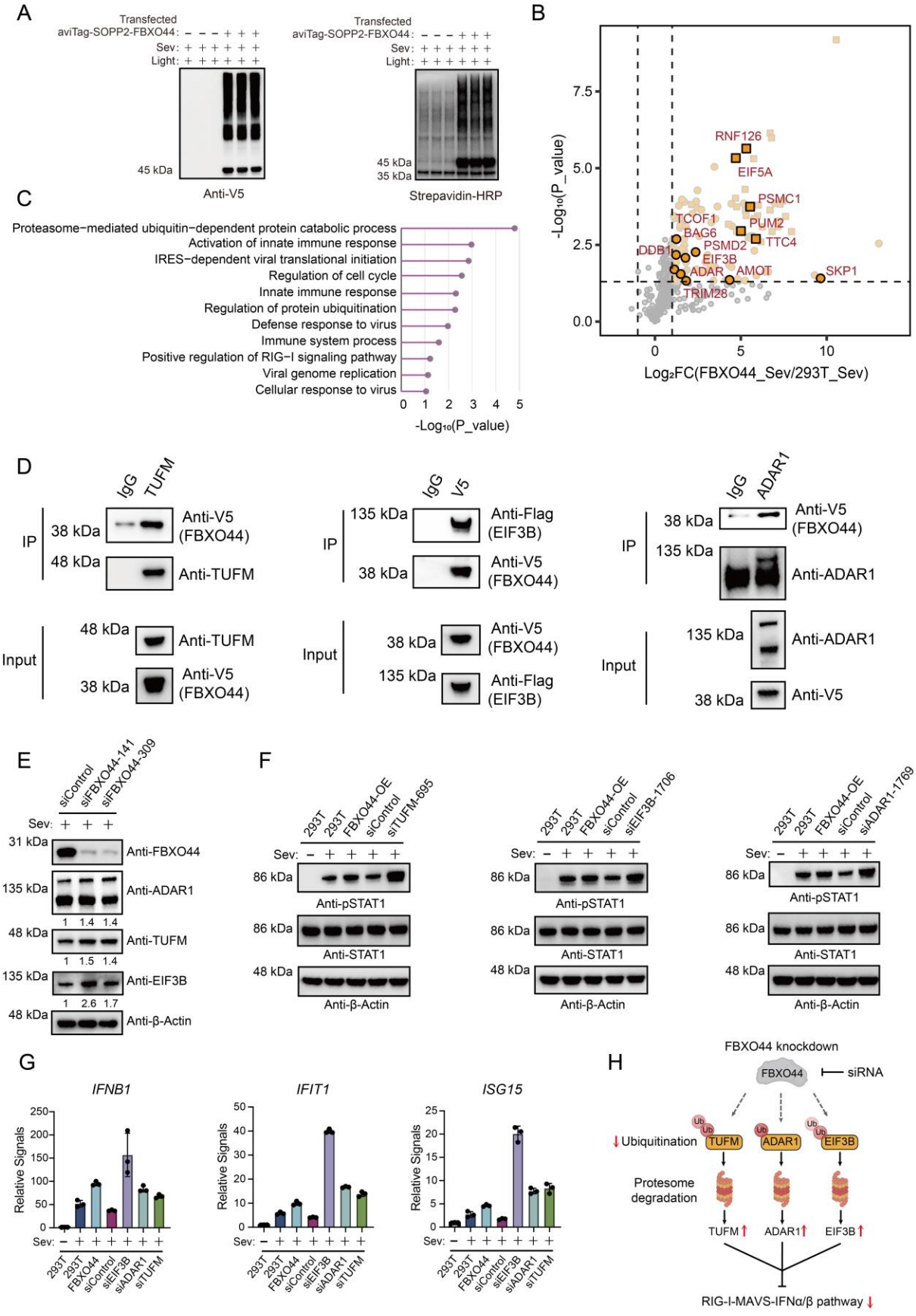

Fig. 7 PZPC maps the FBXO44 proximity network and identifies candidate regulators of antiviral signaling. A) PZPC crosslinking of AviTag–SOPP2–FBXO44 under Sendai virus (SeV) infection. HEK293T cells expressing AviTag–SOPP2–FBXO44 were irradiated with blue light as indicated. Anti-V5 immunoblotting detected high-molecular-weight FBXO44-containing crosslinked species, and streptavidin–HRP blotting confirmed biotinylated products. **B)** Quantitative proteomic analysis of FBXO44-associated proteins identified by PZPC under SeV stimulation. Proteins enriched in the FBXO44 condition relative to SeV-treated control cells are plotted by log2fold change and statistical significance. Statistically significant enriched proteins are shown as circles, and singletons are shown as squares. Proteins annotated as viral infection- or innate immunity-associated factors are highlighted. **C)** Reactome pathway analysis of PZPC-identified FBXO44-associated proteins under SeV treatment. **D)** Co-immunoprecipitation validation of representative FBXO44-associated proteins identified by PZPC. TUFM, ADAR1, and Flag-tagged EIF3B were recovered with V5-tagged FBXO44, with IgG serving as a negative control. **E)** Immunoblot analysis of selected FBXO44-associated proteins following siRNA-mediated FBXO44 knockdown. ADAR1 p150, TUFM and EIF3B showed increased abundance upon FBXO44 depletion. β-Actin was used as a loading control. **F)** Functional assessment of candidate FBXO44-regulated proteins. STAT1 phosphorylation was analyzed by immunoblotting after SeV infection in control cells, FBXO44-overexpressing cells, or cells treated with control siRNA or siRNAs targeting TUFM, EIF3B or ADAR1. Total STAT1 and β-actin were used as controls. **G)** qPCR analysis of *IFNB1, IFIT1,* and *ISG15* expression following SeV infection in control cells, FBXO44-overexpressing cells, or cells knockdown of TUFM, EIF3B or ADAR1. **H)** Working model of FBXO44-mediated antiviral regulation. FBXO44 promotes degradation of TUFM, ADAR1, and EIF3B; FBXO44 knockdown stabilizes these negative regulators and attenuates RIG-I–MAVS–IFNα/β signaling. Experiments were repeated at least twice with similar results.

DISCUSSION

In this study, we establish photocatalytic zero-length proximity crosslinking (PZPC) as a genetically encoded and light-controlled strategy for mapping protein interaction networks in

living cells. By coupling localized photosensitizer-mediated oxidation with POI-restricted biotin enrichment, PZPC enables covalent capture of proximal protein contacts with high spatial and temporal control. Unlike conventional proximity labeling, which relies on diffusible reactive species to label neighboring proteins, PZPC captures protein contacts through covalent crosslinking, thereby providing a more stringent readout of physical proximity. Unlike conventional chemical crosslinking mass spectrometry, PZPC does not require addition of exogenous bifunctional crosslinkers and can be directed to a specific POI as "zero-length" crosslinking in cells. These features make PZPC particularly suitable for interrogating transient, low-stoichiometry and degradation-coupled interactions that are difficult to preserve by affinity purification.

A key technical advance of this work is the development of LinkMasser, a blind-search strategy for discovering unknown crosslink-associated mass offsets from crosslinking mass spectrometry data. Because PZPC is not based on a predefined synthetic crosslinker, the chemical mass of the resulting crosslinked peptide pair cannot be assumed in advance. LinkMasser addresses this problem by searching tandem MS spectra without precursor mass constraints, nominating candidate peptide pairs, calculating residual precursor mass offsets and clustering recurrent offsets to identify candidate crosslink masses. To our knowledge, this represents the first blind-search framework specifically designed to infer unknown crosslink-associated masses. Using LinkMasser, we identified a recurrent +14-Da mass shift, assigned as H(−2)O(+1), consistent with oxidative dehydrogenative coupling. MS/MS data further supported Lys–His crosslinks as a representative chemical signature of PZPC-mediated zero-length crosslinking. Although the precise chemical structure of the crosslink remains to be fully defined, this computational and experimental workflow provides a general route for decoding unknown

crosslinking chemistries directly from proteomic data.

PZPC is complementary to, but distinct from, existing photo-crosslinking and proximity labeling strategies. In the midnolin system, conventional anti-HA AP–MS mainly recovered stable proteasome-associated components, whereas PZPC captured a focused set of inducible transcription factors and other regulatory proteins that are largely missed by standard affinity purification. This distinction is biologically important because midnolin substrates, especially immediate-early transcription factors, are short-lived and degradation-coupled. Recent photo-crosslinking approaches have also been applied to the midnolin system using genetically encoded photo-crosslinking amino acids or residue-selective photo-crosslinkers[56]. While these approaches are powerful, they require careful selection of UAA incorporation sites, amber suppression, or additional crosslinker chemistry. In contrast, PZPC uses a single photosensitizer fusion and avidin-based enrichment design, making the workflow operationally simpler and readily scalable to diverse POIs. In our midnolin application, this design enabled robust capture of these labile regulatory proteins, functional validation of candidate substrates, and discrimination between degradative substrates and non-degradative interactors. Thus, PZPC provides a simple and scalable strategy for mapping dynamic degradation-coupled interaction networks in cells.

We further extended PZPC from individual POIs to family-wide profiling of F-box proteins, a major class of substrate-recognition receptors in SCF ubiquitin ligases. F-box proteins regulate many essential biological processes, including cell-cycle control, protein quality control, stress responses and immune signaling. Recent studies have highlighted the mechanistic richness of individual F-box proteins, such as FBXO42-mediated degradation of PP2A catalytic subunits through a CCDC6-dependent degradosome-like assembly[57], and FBXO31-mediated recognition of C-terminal amide-bearing damaged proteins[58]. These studies underscore that F-box proteins are

not merely interchangeable substrate receptors but can encode highly specialized degron-recognition logic and pathway-specific regulatory mechanisms. In addition, F-box proteins are increasingly being explored as E3 ligases for targeted protein degradation, as exemplified by FBXO31-recruiting terminal amide-functionalized degraders[59]. Therefore, systematic identification of F-box interaction and substrate landscapes is not only important for basic biology, but also for expanding the repertoire of E3 ligases available for therapeutic protein degradation.

Using optimized PZPC conditions, we generated a family-wide proximity atlas covering 63 F-box proteins across the FBXO, FBXL and FBXW subfamilies. This atlas revealed extensive heterogeneity in interaction network size and composition, suggesting that individual F-box proteins differ substantially in their substrate-regulatory capacity. The dataset recovered canonical SCF components, including SKP1, CUL1 and RBX1, validating the platform, but also revealed unexpected connections to CUL4B, CAND1, chaperones, proteasome-associated factors, ER-associated degradation components and other ubiquitin-system regulators. These findings suggest that F-box proteins may function within a broader and more plastic cullin–RING ligase network than the canonical SCF model alone would predict. Functional validation further converted this proximity atlas into a candidate substrate map: among 257 tested candidates, 81 showed reproducible stabilization upon depletion of the corresponding F-box protein. The validated substrates span transcriptional regulation, RNA processing, cytoskeletal organization, metabolism, protein quality control and cell-cycle control. Importantly, the substrate map is selective rather than globally promiscuous, with most substrates linked to only one or a few F-box proteins, while several F-box members function as substrate-rich hubs. This integrated proximity-capture and perturbation workflow provides a scalable strategy for discovering F-box-dependent degradation pathways.

Beyond constructing an atlas, we used this resource to uncover a pathway-specific regulatory mechanism in antiviral signaling. A family-wide ISRE reporter screen nominated FBXO44 as a positive regulator of Sendai virus-induced RIG-I–MAVS signaling. Gain- and loss-of-function experiments showed that FBXO44 enhances STAT1 phosphorylation and promotes induction of antiviral genes, including *IFNB1, IFIT1, ISG15* and *Mx1*. PZPC profiling of FBXO44 under viral infection further revealed an infection-associated proximity network enriched for ubiquitin–proteasome factors and innate immune regulators. Among these, ADAR1, EIF3B and TUFM were stabilized upon FBXO44 depletion and acted as negative regulators of antiviral gene induction. These data support a model in which FBXO44 promotes RIG-I–MAVS–IFN signaling by restraining inhibitory proteins within the antiviral network.

The identification of ADAR1 as a candidate FBXO44-regulated protein is particularly intriguing. The interferon-inducible ADAR1 p150 isoform is approximately 150 kDa and contains an N-terminal Zα domain that distinguishes it from the constitutive p110 isoform[60,61]. ADAR1 p150 has important roles in sensing or editing structured viral and endogenous RNAs and in preventing aberrant activation of innate immune pathways[62,63]. Our data suggest that FBXO44 may enhance antiviral signaling by limiting inducible ADAR1 p150 abundance, thereby relieving an inhibitory brake on the RIG-I–MAVS–IFN axis. In this model, FBXO44-dependent degradation of ADAR1 and other negative modulators such as EIF3B and TUFM would amplify antiviral signaling and potentially enhance viral restriction. Future studies will be needed to define the direct ubiquitination sites, degron features and infection-stage specificity of this regulation, but the current results establish an FBXO44-centered antiviral regulatory circuit uncovered through PZPC-guided discovery.

Together, this work integrates methodological innovation, computational tool development

and biological discovery. Methodologically, PZPC provides a light-controlled, genetically encoded and POI-directed zero-length crosslinking platform for mapping protein interaction networks in living cells. Computationally, LinkMasser enables unbiased discovery of unknown crosslink-associated masses and provides a route to mechanistic annotation of crosslinking chemistry. Biologically, PZPC captured transient midnolin–transcription factor interactions, generated a family-wide F-box proximity and substrate atlas, and uncovered an FBXO44–ADAR1/EIF3B/TUFM antiviral regulatory circuit. Thus, PZPC does not simply catalog proximity interactions; it enables functional reconstruction of dynamic protein networks and degradation pathways. We anticipate that this platform will be broadly useful for studying transient protein interactions, E3 ligase substrate recognition, immune signaling and therapeutically relevant protein degradation systems.

Methods

Cell culture. HEK293T cell line was obtained from ATCC (CRL-3216). All cell lines tested negative for mycoplasma. HEK293T was cultured in DMEM supplemented with 10% fetal bovine serum and 1% penicillin/streptomycin.

Plasmid construction. All genetic constructs used in this study are listed in Supplementary Table 1. Unless otherwise stated, plasmid construction was performed by General Biol. The pET21a-BirA-6×His plasmid was a gift from Prof. Peng Chen's laboratory. The coding sequence of MIDN was synthesized according to the sequence reported previously[31] and subsequently cloned into the pLX304 vector. For knockdown experiment, shRNA targeting MIDN was cloned into the pLKO.1 vector (Supplementary Table 2).

In vitro biotinylation optimization. HEK293T cells stably expressing SOPP3–H2BC11–AviTag were lysed under different conditions to optimize AviTag biotinylation efficiency. Cells were lysed in RIPA lysis buffer (Beyotime, P0013B), PBS, or RIPA lysis buffer followed by dilution with an equal volume of PBS. For PBS-based lysis, cells were disrupted by sonication at 35% amplitude for 1 min using a 1 s on/2 s off cycle. Lysates were clarified by centrifugation, and protein concentrations were determined using a BCA assay. The lysates were then adjusted to 1 mg/mL with the corresponding buffer and subjected to in vitro biotinylation. Biotinylated samples were analyzed by SDS–PAGE and western blotting, and the optimal lysis condition was selected based on the biotinylation signal intensity of SOPP3–H2BC11.

To optimize BirA concentration, in vitro biotinylation was performed using the 1:1 RIPA/PBS lysis condition with BirA at final concentrations of 10, 30, 40 or 400 μg/mL. Samples were analyzed by SDS–PAGE and western blotting. The optimal BirA concentration was determined based on the biotinylation signal of SOPP3–H2BC11 while minimizing BirA self-biotinylation.

PZPC sample preparation and LC-MS/MS analysis. To identify POI-associated proteins by PZPC, parental HEK293T cells were used as blank controls, and stable or transiently transfected cells were assigned to light-treated and dark-control groups. Unless otherwise stated, three biological replicates were prepared for each condition. Cells were cultured in 10-cm dishes to approximately 90% confluence and treated with MG132 (10 μM final concentration; Macklin, M832899) for 6 h before harvest. Additional treatment conditions are described in the corresponding figure legends. Cells were then washed twice with HBSS. For light-treated samples, cells were irradiated with blue LED light at 450 nm for 10 min in fresh HBSS. Dark-control samples were kept protected from light throughout the procedure. Cells were then collected in ice-cold PBS and lysed in RIPA buffer supplemented with EDTA-free protease inhibitor cocktail (MCE, HY-K0011) on ice for 30 min. Lysates were briefly sonicated to reduce viscosity and clarified by centrifugation at 13,000 × g for 10 min at 4 °C. Protein concentrations were determined using a BCA assay (Beyotime, P0009). For each sample, 2 mg of total protein was adjusted to 8 mg/mL in RIPA

buffer in a final volume of 250 μL and then diluted with an equal volume of PBS containing protease inhibitor cocktail to a final concentration of 4 mg/mL. A small portion of each lysate was retained as input for western blot analysis to assess light-induced crosslinking.

For in vitro biotinylation of AviTag-fused proteins, ATP (Beyotime, D7378), $MgCl_2$, D-biotin (Sangon, A100340) and BirA were added to lysates at final concentrations of 2 mM, 5 mM, 10 μM and 40 μg/mL, respectively. Samples were incubated overnight at 25 °C with shaking. After biotinylation, proteins were precipitated using a methanol/chloroform/water mixture (4:1:3.5 mL), followed by centrifugation at 4,500 × g for 10 min at room temperature. Protein pellets were washed twice with 1 mL methanol and resuspended in 1 mL of 8 M urea in 50 mM ammonium bicarbonate (ABC) buffer. A portion of each sample was analyzed by western blotting to confirm biotinylation efficiency.

Proteins were reduced with 10 μL DTT at a final concentration of 10 mM at 55 °C for 40 min and alkylated with 50μL iodoacetamide at a final concentration of 15 mM in the dark at room temperature for 30 min. Alkylation was quenched by adding 5 μL DTT to a final concentration of 5 mM. Samples were diluted with 4 mL PBS and incubated with 50 μL pre-washed NeutrAvidin agarose resin (Thermo Fisher Scientific, 29204) for 4 h at room temperature. Beads were washed three times with 5 mL PBS containing 0.2% SDS, three times with 5 mL PBS containing 1 M urea and three times with 5 mL PBS. Beads were then resuspended in 300 μL of 25 mM ABC buffer containing 1 M urea, 1 mM $CaCl_2$ and 20 ng/μL trypsin, and on-bead digestion was performed overnight at 37 °C with shaking. After centrifugation at 8,000 rpm for 5 min, the peptide-containing supernatant was collected and acidified to pH 2-3 with 20% formic acid. Peptides were desalted using a SOLAμ SPE plate (Thermo Fisher Scientific, 60309-001), dried in a vacuum concentrator at 37 °C and reconstituted in 10 μL of 0.1% formic acid in water. Peptide concentration was estimated using a NanoDrop spectrophotometer.

For LC–MS/MS analysis, 500 ng peptides were analyzed on a Q Exactive Plus mass spectrometer equipped with a nano-ESI source and operated using Xcalibur 4.3 software. Peptides were separated on a 150 μm × 20 cm capillary column packed with 1.9 μm C18 resin using an EASY-nLC 1200 UHPLC system.

Peptides were eluted at a flow rate of 300 nL/min using a 95-min linear gradient from 8% to 50% solvent B, followed by a 6-min ramp to 98% solvent B. Solvent A was 0.1% formic acid in water, and solvent B was 0.1% formic acid in 80% acetonitrile. Data were acquired in data-dependent acquisition (DDA) mode. Full MS scans were acquired over an m/z range of 350-2,000 at a resolution of 120,000, with an AGC target of 4×10^5 and a maximum injection time of 150 ms. The spray voltage was set to 2.0 kV, and the ion transfer capillary temperature was 320 °C. The top 10 most abundant precursor ions were selected for HCD fragmentation at 30% normalized collision energy with a quadrupole isolation window of 1.6 m/z. MS/MS scans were acquired at a resolution of 30,000, with an AGC target of 5×10^4 and a maximum injection time of 150 ms. Dynamic exclusion was set to 30 s. Ions with charge states of 1+ or >7+ were excluded from MS/MS analysis.

Raw files were processed using Proteome Discoverer with a label-free quantification workflow. Protein abundance values were exported for downstream analysis using an in-house R package. Endogenously biotinylated proteins, including pyruvate carboxylase (PC), methylcrotonoyl-CoA carboxylase 1 (MCCC1), propionyl-CoA carboxylase alpha subunit (PCCA) and acetyl-CoA carboxylase alpha (ACACA), were used for normalization. Differentially enriched proteins were identified based on fold change and statistical significance. Proteins with fold change ≥ 2 and $P < 0.05$ were considered significantly enriched and defined as candidate POI-interacting proteins. Volcano plots were generated using $\log_2$fold change and $-\log_{10}$P value.

Plasmid and siRNA transfection. HEK293T cells were seeded in the indicated culture dishes and transfected at 50-70% confluence using Lipo8000 transfection reagent (Beyotime, C0533). For each 10-cm dish, 15 μg of plasmid DNA was diluted in 750 μL Opti-MEM and mixed with 24 μL Lipo8000 reagent. After incubation at room temperature for 10 min to allow lipid–DNA complex formation, the mixture was added dropwise to cells in fresh complete medium. The medium was replaced with fresh complete medium after 24 h, and cells were harvested 36-48 h after transfection.

For siRNA transfection, HEK293T cells were seeded in antibiotic-free growth medium one day before transfection and transfected at 30-50% confluence using Lipofectamine RNAiMAX transfection reagent (Thermo Fisher Scientific, 13778150). siRNA and RNAiMAX were diluted separately in Opti-MEM, combined and incubated at room temperature for 10-20 min to allow siRNA–lipid complex formation. The complexes were then added dropwise to cells to achieve a final siRNA concentration of 16 nM. Cells were harvested 48-72 h after transfection for knockdown analysis or downstream experiments. All siRNA sequences used in this study are listed in Supplementary Table 2.

Stable cell line generation. For stable overexpression cell line generation, HEK293T cells were plated at 2.0×10^5 cells per well in 6-well plates. After 24 h, cells at approximately 80% confluence were transfected with 2.4 μg recombinant lentiviral plasmid based on the pLX-304 backbone, together with packaging plasmids psPAX2 and pMD2.G at 3 μg and 1 μg, respectively, using Lipo8000 transfection reagent. The medium was replaced with fresh complete medium 24 h after transfection. Viral supernatants were collected 48 h later and filtered through a 0.45-μm filter. The filtered viral supernatant was used to transduce HEK293T cells, followed by selection with blasticidin at 5 μg/mL for at least 7 days. Overexpression was confirmed by western blotting.

For stable knockdown cell line generation, HEK293T cells were plated at 2.0×10^5 cells per well in 6-well plates. After 24 h, cells at approximately 80% confluence were transfected with 2.4 μg recombinant lentiviral plasmid based on the pLKO backbone, together with 3 μg psPAX2 and 1 μg pMD2.G, using Lipo8000 transfection reagent. The medium was replaced with fresh complete medium 24 h after transfection. Viral supernatants were collected 48 h later, filtered through a 0.45-μm filter and used to transduce HEK293T cells. Transduced cells were selected with puromycin at 2 μg/mL for at least 7 days, and knockdown efficiency was validated by qPCR.

Western blot analysis. For western blot validation of mass spectrometry results from the 63 F-box protein datasets, input and biotin-enriched samples were separated by SDS–PAGE and transferred onto PVDF membranes. Input samples were incubated with anti-V5 antibody (Cell Signaling Technology, 80076) overnight at 4 °C, followed by incubation with the appropriate HRP-conjugated secondary antibodies. Biotin-enriched samples were detected using streptavidin–HRP (Solarbio, SE068). Protein bands were visualized using enhanced chemiluminescence. Detailed information for all antibodies used in this study is provided in Supplementary Table 3.

Purification of recombinant BirA from *E. coli*. For prokaryotic expression, the pET21a-BirA-6×His plasmid was transformed into Escherichia coli BL21(DE3) competent cells. Transformed cells were cultured in LB medium supplemented with ampicillin at 50 μg/mL at 37 °C until the optical density at 600 nm reached approximately 0.6. Protein expression was induced with 0.1 mM IPTG at 20 °C for 14 h with shaking. Cells were harvested by centrifugation at 4,000 × g for 10 min at 4 °C and lysed in buffer A containing 20 mM Tris-HCl, 150 mM NaCl and 1 mM DTT, pH 7.5, supplemented with protease inhibitor cocktail. Cell lysis was performed using a high-pressure homogenizer. The lysate was clarified by centrifugation, and the supernatant was applied to Ni-NTA agarose resin for affinity purification. The resin was washed with 50 mL wash buffer containing 50 mM imidazole, 20 mM Tris-HCl, 150 mM NaCl and 1 mM DTT, pH 7.5. Bound proteins were eluted stepwise with wash buffer containing 100, 150 or 250 mM imidazole. Protein-containing fractions were pooled and further purified by size-exclusion chromatography (Cytiva, 28990944). Fractions with purity ⩾95% were collected, buffer-exchanged into storage buffer containing 50 mM imidazole, 50 mM NaCl, 5% glycerol and 5 mM β-mercaptoethanol, pH 6.8, aliquoted, flash-frozen in liquid nitrogen and stored at −80 °C.

Co-immunoprecipitation and western blot analysis. HEK293T cells were transiently transfected with

the indicated V5-tagged F-box expression plasmids. After 48 h, cells were washed with PBS and lysed in IP lysis buffer (Thermo Fisher Scientific, 87787) supplemented with protease inhibitor cocktail. Cell lysates were clarified by centrifugation, and 1 mg of total protein was used for each immunoprecipitation. Lysates were incubated overnight at 4 °C with antibodies against the indicated interacting proteins, followed by incubation with Protein A/G magnetic beads (Yeasen, 36417ES08) for 1 h at 4 °C. The beads were washed three times with NP-40 buffer containing 1% NP-40, 150 mM NaCl and 50 mM HEPES, pH 7.6, followed by one wash with RIPA buffer. Bound proteins were eluted in 2× SDS loading buffer by heating at 95 °C for 10 min, and co-precipitated V5-tagged F-box proteins were detected by western blotting.

For interaction analysis of EIF3B or ADAR1 with FBXO44, cells were transiently co-transfected with V5-FBXO44 and 3×Flag-tagged EIF3B or ADAR1 expression plasmids, because the corresponding endogenous antibodies were not suitable for efficient immunoprecipitation. Cell lysates were immunoprecipitated with anti-Flag antibody, and co-precipitated V5-FBXO44 was detected by western blotting. For western blot analysis, samples were resolved by SDS–PAGE and transferred onto PVDF membranes. Membranes were incubated with the indicated primary antibodies at the recommended dilutions overnight at 4 °C, followed by HRP-conjugated secondary antibodies (TransGen) at 1:5,000. Protein bands were visualized using enhanced chemiluminescence.

Immunofluorescence imaging. HEK293T cell lines stably expressing H2BC11 or Lamin A constructs were seeded into 35-mm confocal dishes at approximately 5×10^5 cells per dish. After 24 h, cells were washed twice with PBS and fixed with 4% formaldehyde (Sangon, E672002) for 15 min at room temperature. Cells were washed three times with PBS and permeabilized with 0.25% Triton X-100 in PBS for 30 min. After three additional PBS washes, cells were blocked with 5% BSA in PBST, consisting of PBS containing 0.1% Tween-20, for 2 h at room temperature. Primary antibodies diluted in 5% BSA in PBST were added to the central glass well of each dish and incubated overnight at 4 °C. Cells were then washed three times with PBST and incubated with the corresponding fluorophore-conjugated secondary

antibodies for 1 h at room temperature in the dark. After washing, nuclei were stained with Hoechst at 5 μg/mL in PBST for 15 min. Cells were washed three final times with PBST and maintained in PBS before imaging. Immunofluorescence images were acquired using a ZEISS LSM 980 confocal microscope with ZEN 3.5 software.

RT-qPCR analysis. For validation of shRNA- or siRNA-mediated knockdown efficiency, total RNA was extracted from the indicated cells using RNAiso Plus reagent (TaKaRa, 9109). Genomic DNA removal and reverse transcription were performed using the FastKing cDNA First-Strand Synthesis Kit (TIANGEN, KR116-01). Quantitative PCR was performed using SYBR Green Pro Taq HS Premix (Accurate Biology, AG11718) on a real-time PCR system, with fluorescence detection at 60 °C. Relative gene expression levels were normalized to GAPDH as the internal control.

To examine genes involved in the RIG-I–MAVS signaling pathway, HEK293T cells were transfected with the indicated plasmids or siRNAs for 42 h, followed by Sendai virus (SeV) infection for 12 h. Cells were then collected for RNA extraction, reverse transcription and qPCR analysis as described above. All qPCR primers used in this study are listed in Supplementary Table 2.

Validation of midnolin-interacting proteins. HEK293T cells stably expressing SOPP2–MIDN were cultured to approximately 90% confluence and treated with MG132 at 10 μM (final concentration) and PMA (Sangon, A606759) at 20 ng/mL (final concentration) for 6 h. Cells were then washed with PBS and subjected to blue-light irradiation in HBSS. Dark-control samples were kept protected from light throughout the procedure. After treatment, cells were collected and lysed in RIPA buffer supplemented with protease inhibitor cocktail.

Lysates were briefly sonicated and diluted with an equal volume of PBS to generate a 1:1 RIPA/PBS lysis condition. A portion of each lysate was retained as input, and the remaining lysates were subjected to

in vitro biotinylation, protein precipitation, reduction, alkylation and NeutrAvidin enrichment as described above. Bound proteins were eluted with 2× SDS loading buffer and analyzed by western blotting using antibodies against the indicated candidate interacting proteins.

In vivo ubiquitination assay. HEK293T cells were transiently co-transfected with the indicated expression plasmids, including V5-FBXO44, EIF3B-3×Flag, TUFM-Flag or ADAR1-3×Flag, together with HA-tagged ubiquitin (HA-Ub). At 36 h after transfection, cells in the virus-treated groups were infected with SeV for 12 h. Before harvest, cells were treated with MG132 at a final concentration of 10 μM for 6 h to inhibit proteasomal degradation. Cells were then lysed in IP lysis buffer supplemented with protease inhibitor cocktail. Lysates were clarified by centrifugation, and the supernatants were incubated with 3 μg anti-HA antibody overnight at 4 °C, followed by incubation with Protein A/G magnetic beads for 1 h at 4 °C. The beads were washed three times with NP-40 buffer and once with RIPA buffer. Bound proteins were eluted in 2× SDS loading buffer by heating at 95 °C for 10 min, and the eluates were analyzed by western blotting with the indicated antibodies.

Substrate identification assay. To analyze potential MIDN substrates, HEK293T cells, MIDN-overexpressing cells and shMIDN cells were lysed in RIPA buffer supplemented with protease inhibitor cocktail. Lysates were quantified by BCA assay and normalized across samples. Samples were mixed with SDS loading buffer, denatured at 95 °C for 10 min, separated by SDS–PAGE and analyzed by western blotting using the indicated antibodies.

To analyze potential F-box protein substrates, HEK293T cells were transfected with three independent siRNAs targeting distinct regions of each indicated F-box gene. Knockdown efficiency was assessed by western blotting or RT–qPCR. Cells were harvested 48–72 h after transfection, lysed and analyzed by western blotting as described above. Proteins showing reproducible increases in abundance

upon depletion of the corresponding F-box protein were considered candidate F-box-regulated substrates.

CHX chase assay. To determine protein degradation kinetics, siRNA-transfected HEK293T cells and control cells were treated with cycloheximide (CHX; MCE, HY-12320) at a final concentration of 75 μg/mL 48 h after transfection to inhibit de novo protein synthesis. Cells were harvested at the indicated time points after CHX treatment and lysed in RIPA buffer supplemented with protease inhibitor cocktail. Lysates were clarified by centrifugation and protein concentrations were determined using a BCA assay. Equal amounts of protein were mixed with SDS loading buffer, denatured at 95 °C for 10 min and analyzed by western blotting using the indicated antibodies.

Serum stimulation assay. HEK293T cells and MIDN-overexpressing cells were cultured separately in 6-cm dishes. At approximately 70% confluence, cells were serum-starved in FBS-free DMEM for 12–16 h and then stimulated with DMEM containing 20% FBS. Cells were harvested at 0, 0.5, 1, 2, 4 and 6 h after stimulation and lysed in RIPA buffer supplemented with protease inhibitor cocktail. Lysates were quantified by BCA assay and normalized across samples. Equal amounts of protein were analyzed by western blotting using the indicated antibodies.

ROS species analysis. HEK293T cells stably expressing miniSOG–Lamin A, SOPP2–Lamin A or SOPP3–Lamin A were cultured in 6-cm dishes to approximately 90% confluence. Cells were washed twice with HBSS and incubated for 1 h with the indicated ROS scavengers or modulators diluted in HBSS. Unless otherwise indicated, the following final concentrations were used: 10 mM sodium azide, 100 mM D-mannitol, 5 mM Trolox, 0.5 mM vitamin C, 100 μM H_2O_2, or D_2O-containing buffer. After reagent incubation, light-treated samples were irradiated with blue LED light at 450 nm for 10 min, whereas control samples were kept in the dark. Cells were then washed twice with HBSS and lysed in RIPA buffer

supplemented with protease inhibitor cocktail. Lysates were quantified by BCA assay, normalized to 1 mg/mL, mixed with SDS loading buffer, denatured at 95 °C for 10 min and analyzed by western blotting using the indicated antibodies.

Optimization of SeV infection duration. HEK293T cells transiently transfected with FBXO44 were infected with SeV for 0, 3, 6, 9 or 12 h at 36 h after transfection. For western blot analysis, cells were lysed in RIPA buffer supplemented with protease inhibitor cocktail and phosphatase inhibitors, followed by immunoblotting for pSTAT1 and total STAT1. For qPCR analysis, total RNA was extracted using RNAiso Plus and analyzed by RT–qPCR as described above.

ISRE-luciferase reporter screening assay. HEK293T cells stably expressing Renilla and ISRE-driven firefly luciferase reporters were plated in 96-well plates at 5–6 × 10^4 cells per well 24 h before transfection. Cells were transfected with the indicated F-box expression plasmids at 70–80% confluence. At 8 h after transfection, cells were infected with SeV for 18 h and then lysed with 1× Passive Lysis Buffer. Reporter activity was measured using the Dual-Luciferase Reporter Assay System (Promega, E1960) according to the manufacturer's instructions. Cell lysates were transferred to white 96-well plates, and firefly luciferase activity was first measured after addition of Luciferase Assay Reagent II. Stop & Glo Reagent was then added to quench the firefly luciferase signal and measure Renilla luciferase activity. Relative ISRE-luciferase activity was normalized to Renilla activity, and fold changes were calculated relative to the SeV-treated vector control.

Western blot analysis of RIG-I-MAVS pathway related proteins. HEK293T cells were transfected with the indicated plasmids or siRNAs for 42 h and then infected with SeV for 12 h. Cells were lysed in RIPA buffer supplemented with protease inhibitor cocktail and phosphatase inhibitors. Lysates were clarified by

centrifugation and protein concentrations were determined by BCA assay. Equal amounts of protein were mixed with SDS loading buffer, denatured, resolved by SDS–PAGE and analyzed by western blotting for pSTAT1 and total STAT1.

LinkMasser benchmarking and PZPC data analysis. The indexing and scoring procedures in LinkMasser were based on pLink3. The filtering of candidate peptides comprised the following steps: (1) Score thresholding: a minimum score threshold was applied to candidates from each spectrum, and the top-scoring candidate within that spectrum was additionally required to exceed a second threshold. Spectra with fewer than two remaining candidate peptides after filtering were discarded. (2) Entrapment database filtering: candidate sequences were removed if they inferred from decoy proteins or entrapment other than the original target proteins. (3) Precursor ion filtering: for each scan, only the highest-scoring precursor ion was kept, and an average amino acid model similarity score >0.8 was required. (4) Filtering of low-confidence cross-linked candidate pairs: pairs in which one peptide was an exact substring of the other were removed. DBSCAN clustering was implemented using the Python scikit-learn package, version 1.6.1.

For the LinkMasser benchmarking evaluation, six datasets were used: DSS and DSBU cross-linking data were obtained from PXD014337[64], while DSSO, CDI, ADH, and DSBSO data were obtained from PXD029252[65]. The FASTA databases provided in the original studies were used. For blind searches, the peptide length range was set to 6–60 residues and the peptide mass range to 600–6,000 Da. Trypsin digestion was specified with up to three missed cleavages. Carbamidomethylation of Cys was set as a fixed modification, oxidation of Met was set as a variable modification and the fragment-ion mass tolerance was set to 10 ppm.

For analysis of the PZPC data, pFind3 version 3.2.3 and pLink3 version 3.1.4 were used. pFind3 was used to search linear peptides against a human proteome FASTA database (UniProt, downloaded Nov. 23, 2023) that contained the POI protein sequence fused with the photosensitizer and the enrichment tag. In addition to the parameters described above, the precursor mass tolerance was set to 10 ppm and the

fragment-ion mass tolerance to 20 ppm. A closed search was performed, with the false discovery rate (FDR) controlled at 1% at the peptide level. pLink3 was then used to search cross-linked peptide pairs. The FASTA database for pLink3 was constructed from the pFind3 results and included only proteins supported by at least two linear peptide sequences. The specific crosslinker mass was obtained via LinkMasser. In addition to the parameters described above, the precursor mass tolerance was set to 10 ppm and the fragment-ion mass tolerance to 10 ppm, with the 1% FDR controlled at peptide-pair-level. Annotated cross-linked spectra were visualized using pLabel. Protenix (model version protenix_base_20250630_v1.0.0) was run at https://protenix-server.com.

AlphaFold-Multimer prediction and model evaluation. For AlphaFold-Multimer analysis, candidate interacting protein pairs were modeled using AlphaFold2 v2.3.2 with the multimer pipeline. The protein sequences were prepared as paired FASTA files and submitted to a GPU-based computing cluster through a SLURM shell script. AlphaFold generated ranked PDB structures for each protein pair, which were subsequently analyzed with custom scripts to calculate pLDDT and BSASA values. Prediction quality was assessed based on both global model confidence and interface burial, with pLDDT > 50 and BSASA > 500 $Å^2$ used as empirical cutoffs for selecting plausible interaction models.

AlphaFold3 prediction of substrate β-strand binding to midnolin. Complex structures between midnolin and candidate substrates were predicted using AlphaFold3 via the AlphaFold Server. For each prediction, the midnolin sequence and the candidate substrate sequence were submitted as separate protein chains in JSON format, with one copy of each chain. The predicted models were analyzed to determine whether the interacting protein adopted a β-strand upon binding to midnolin and whether this β-strand inserted into the midnolin Catch domain.

Data availability

The mass spectrometry data generated in this study have been deposited to the ProteomeXchange Consortium via the iProX[66] partner repository. Source data are provided with this paper.

Code availability

The python code and the corresponding dataset have been deposited to Zenodo with https://doi.org/10.5281/zenodo.20225636. Alternatively, it is available from the G.L. upon request.

References

1 Larance, M. & Lamond, A. I. Multidimensional proteomics for cell biology. *Nat Rev Mol Cell Biol* **16**, 269-280, doi:10.1038/nrm3970 (2015).

2 Huttlin, E. L. *et al.* Dual proteome-scale networks reveal cell-specific remodeling of the human interactome. *Cell* **184**, 3022-3040 e3028, doi:10.1016/j.cell.2021.04.011 (2021).

3 Bonetta, L. Protein-protein interactions: Tools for the search. *Nature* **468**, 852, doi:10.1038/468852a (2010).

4 Gingras, A. C., Abe, K. T. & Raught, B. Getting to know the neighborhood: using proximity-dependent biotinylation to characterize protein complexes and map organelles. *Curr. Opin. Chem. Biol.* **48**, 44-54, doi:10.1016/j.cbpa.2018.10.017 (2019).

5 Zhou, Y. & Zou, P. The evolving capabilities of enzyme-mediated proximity labeling. *Curr Opin Chem Biol* **60**, 30-38, doi:10.1016/j.cbpa.2020.06.013 (2021).

6 McCutcheon, D. C., Lee, G., Carlos, A., Montgomery, J. E. & Moellering, R. E. Photoproximity Profiling of Protein-Protein Interactions in Cells. *J. Am. Chem. Soc.* **142**, 146-153, doi:10.1021/jacs.9b06528 (2020).

7 Yang, B. *et al.* Proximity-enhanced SuFEx chemical cross-linker for specific and multitargeting cross-linking mass spectrometry. *Proc. Natl. Acad. Sci. U S A* **115**, 11162-11167, doi:10.1073/pnas.1813574115 (2018).

8 Liu, J., Yang, B. & Wang, L. Residue selective crosslinking of proteins through photoactivatable or proximity-enabled reactivity. *Curr Opin Chem Biol* **74**, 102285, doi:10.1016/j.cbpa.2023.102285 (2023).

9 Rhee, H. W. *et al.* Proteomic mapping of mitochondria in living cells via spatially restricted enzymatic tagging. *Science* **339**, 1328-1331, doi:10.1126/science.1230593 (2013).

10 Roux, K. J., Kim, D. I., Raida, M. & Burke, B. A promiscuous biotin ligase fusion protein identifies proximal and interacting proteins in mammalian cells. *J. Cell Biol.* **196**, 801-810, doi:10.1083/jcb.201112098 (2012).

11 Branon, T. C. *et al.* Efficient proximity labeling in living cells and organisms with TurboID. *Nat. Biotechnol.* **36**, 880-887, doi:10.1038/nbt.4201 (2018).

12 Zheng, F., Yu, C., Zhou, X. & Zou, P. Genetically encoded photocatalytic protein labeling enables spatially-resolved profiling of intracellular proteome. *Nat Commun* **14**, 2978, doi:10.1038/s41467-023-38565-8 (2023).

13 Hananya, N., Ye, X., Koren, S. & Muir, T. W. A genetically encoded photoproximity labeling approach for mapping protein territories. *Proc Natl Acad Sci U S A* **120**, e2219339120, doi:10.1073/pnas.2219339120 (2023).

14 Zhai, Y. *et al.* Spatiotemporal-resolved protein networks profiling with photoactivation dependent proximity labeling. *Nat Commun* **13**, 4906, doi:10.1038/s41467-022-32689-z (2022).

15 Geri, J. B. *et al.* Microenvironment mapping via Dexter energy transfer on immune cells. *Science* **367**, 1091-1097, doi:10.1126/science.aay4106 (2020).

16 Seath, C. P., Trowbridge, A. D., Muir, T. W. & MacMillan, D. W. C. Reactive intermediates for interactome mapping. *Chem. Soc. Rev.* **50**, 2911-2926, doi:10.1039/d0cs01366h (2021).

17 Lobingier, B. T. *et al.* An Approach to Spatiotemporally Resolve Protein Interaction Networks in Living Cells. *Cell* **169**, 350-360.e312, doi:10.1016/j.cell.2017.03.022 (2017).

18 Oakley, J. V. *et al.* Radius measurement via super-resolution microscopy enables the development of a variable radii proximity labeling platform. **119**, e2203027119, doi:doi:10.1073/pnas.2203027119 (2022).

19 Larios, J. M., Budhiraja, R., Fanburg, B. L. & Thannickal, V. J. Oxidative protein cross-linking reactions involving L-tyrosine in transforming growth factor-beta1-stimulated fibroblasts. *J Biol Chem* **276**, 17437-17441, doi:10.1074/jbc.M100426200 (2001).

20 Barroso-Gomila, O. *et al.* BioE3 identifies specific substrates of ubiquitin E3 ligases. *Nat Commun* **14**, 7656, doi:10.1038/s41467-023-43326-8 (2023).

21 Tamura, T., Takato, M., Shiono, K. & Hamachi, I. Development of a Photoactivatable Proximity Labeling Method for the Identification of Nuclear Proteins. *Chem. Lett.* **49**, 145-148, doi:10.1246/cl.190804 (2020).

22 Wheat, A. *et al.* Protein interaction landscapes revealed by advanced in vivo cross-linking-mass spectrometry. *Proc Natl Acad Sci U S A* **118**, doi:10.1073/pnas.2023360118 (2021).

23 O'Reilly, F. J. & Rappsilber, J. Cross-linking mass spectrometry: methods and applications in structural, molecular and systems biology. *Nat Struct Mol Biol* **25**, 1000-1008, doi:10.1038/s41594-018-0147-0 (2018).

24 Piersimoni, L., Kastritis, P. L., Arlt, C. & Sinz, A. Cross-Linking Mass Spectrometry for Investigating Protein Conformations and Protein-Protein Interactions horizontal line A Method for All Seasons. *Chem Rev* **122**, 7500-7531, doi:10.1021/acs.chemrev.1c00786 (2022).

25 Yu, C. & Huang, L. New advances in cross-linking mass spectrometry toward structural systems biology. *Curr Opin Chem Biol* **76**, 102357, doi:10.1016/j.cbpa.2023.102357 (2023).

26 Ester, M., Kriegel, H., Sander, J. & Xu, X. A density-based algorithm for discovering clusters in large spatial databases with noise. *KDD'96: Proceedings of the Second International Conference on Knowledge Discovery and Data Mining*, 226-231 (1996).

27 Chi, H. *et al.* Comprehensive identification of peptides in tandem mass spectra using an efficient open search engine. *Nature Biotechnology* **36**, 1059-1061, doi:10.1038/nbt.4236 (2018).

28 Guo, H. *et al.* LipoID profiles lipid droplet interactions and identifies interorganelle regulators. *Nat Chem Biol*, doi:10.1038/s41589-025-02127-4 (2026).

29 Ahn, J. *et al.* Structural basis for lamin assembly at the molecular level. *Nat Commun* **10**, 3757, doi:10.1038/s41467-019-11684-x (2019).

30 Zhang, Y. *et al.* Protenix-v1: Toward High-Accuracy Open-Source Biomolecular Structure Prediction. *Bio Archiv.*, doi:https://doi.org/10.64898/2026.02.05.703733 (2026).

31 Gu, X. *et al.* The midnolin-proteasome pathway catches proteins for ubiquitination-independent degradation. *Science* **381**, eadh5021, doi:10.1126/science.adh5021 (2023).

32 Skaar, J. R., Pagan, J. K. & Pagano, M. SCF ubiquitin ligase-targeted therapies. *Nat Rev Drug Discov* **13**, 889-903, doi:10.1038/nrd4432 (2014).

33 Feng, T., Wang, P. & Zhang, X. Skp2: A critical molecule for ubiquitination and its role in cancer. *Life Sciences* **338**, 122409, doi:https://doi.org/10.1016/j.lfs.2023.122409 (2024).

34 Zheng, J. *et al.* CAND1 Binds to Unneddylated CUL1 and Regulates the Formation of SCF Ubiquitin E3 Ligase Complex. *Molecular cell* **10**, 1519-1526, doi:https://doi.org/10.1016/S1097-2765(02)00784-0 (2002).

35 Liu, J., Furukawa, M., Matsumoto, T. & Xiong, Y. NEDD8 Modification of CUL1 Dissociates p120CAND1, an Inhibitor of CUL1-SKP1 Binding and SCF Ligases. *Molecular cell* **10**, 1511-1518, doi:https://doi.org/10.1016/S1097-2765(02)00783-9 (2002).

36 Pierce, Nathan W. *et al.* Cand1 Promotes Assembly of New SCF Complexes through Dynamic Exchange of F Box Proteins. *Cell* **153**, 206-215, doi:10.1016/j.cell.2013.02.024 (2013).

37 Royle, S. J., Bright, N. A. & Lagnado, L. Clathrin is required for the function of the mitotic spindle. *Nature* **434**, 1152-1157, doi:10.1038/nature03502 (2005).

38 Zhao, X. *et al.* The HECT-domain ubiquitin ligase Huwe1 controls neural differentiation and proliferation by destabilizing the N-Myc oncoprotein. *Nature Cell Biology* **10**, 643-653, doi:10.1038/ncb1727 (2008).

39 Han, X. *et al.* Destabilizing LSD1 by Jade-2 Promotes Neurogenesis: An Antibraking System in Neural Development. *Molecular cell* **55**, 482-494, doi:https://doi.org/10.1016/j.molcel.2014.06.006 (2014).

40 Apriamashvili, G. *et al.* Ubiquitin ligase STUB1 destabilizes IFNγ-receptor complex to suppress tumor IFNγ signaling. *Nature Communications* **13**, 1923, doi:10.1038/s41467-022-29442-x (2022).

41 Corcoran, C. A. *et al.* Identification and Characterization of Two Novel Isoforms of Pirh2 Ubiquitin Ligase That Negatively Regulate p53 Independent of RING Finger Domains*. *Journal of Biological Chemistry* **284**, 21955-21970, doi:https://doi.org/10.1074/jbc.M109.024232 (2009).

42 Pérez-Oliva, A. B., Olivares, C., Jiménez-Cervantes, C. & García-Borrón, J. C. Mahogunin Ring Finger-1 (MGRN1) E3 Ubiquitin Ligase Inhibits Signaling from Melanocortin Receptor by Competition with Gαs*. *Journal of Biological Chemistry* **284**, 31714-31725, doi:https://doi.org/10.1074/jbc.M109.028100 (2009).

43 Lam, S. T. T. & Lim, C. J. in *Cellular Biology of the Endoplasmic Reticulum* (eds Luis B. Agellon & Marek Michalak) 181-196 (Springer International Publishing, 2021).

44 Kozlov, G. & Gehring, K. Calnexin cycle – structural features of the ER chaperone system. *The FEBS Journal* **287**, 4322-4340, doi:https://doi.org/10.1111/febs.15330 (2020).

45 Wu, S. A., Li, Z. J. & Qi, L. Endoplasmic reticulum (ER) protein degradation by ER-associated degradation and ER-phagy. *Trends in Cell Biology* **35**, 576-591, doi:https://doi.org/10.1016/j.tcb.2025.01.002 (2025).

46 Wang, Q. *et al.* A Ubiquitin Ligase-Associated Chaperone Holdase Maintains Polypeptides in Soluble States for Proteasome Degradation. *Molecular cell* **42**, 758-770, doi:https://doi.org/10.1016/j.molcel.2011.05.010 (2011).

47 Ishimoto, K. *et al.* Degradation of human Lipin-1 by BTRC E3 ubiquitin ligase. *Biochem Biophys Res Commun* **488**, 159-164, doi:10.1016/j.bbrc.2017.04.159 (2017).

48 Mavrommati, I. *et al.* β-TrCP- and Casein Kinase II-Mediated Degradation of Cyclin F Controls Timely Mitotic Progression. *Cell Rep* **24**, 3404-3412, doi:10.1016/j.celrep.2018.08.076 (2018).

49 Li, J., Chai, Q. Y. & Liu, C. H. The ubiquitin system: a critical regulator of innate immunity and pathogen-host interactions. *Cell Mol Immunol* **13**, 560-576, doi:10.1038/cmi.2016.40 (2016).

50 Bhoj, V. G. & Chen, Z. J. Ubiquitylation in innate and adaptive immunity. *Nature* **458**, 430-437, doi:10.1038/nature07959 (2009).

51 Onomoto, K., Onoguchi, K. & Yoneyama, M. Regulation of RIG-I-like receptor-mediated signaling: interaction between host and viral factors. *Cellular & Molecular Immunology* **18**, 539-555, doi:10.1038/s41423-020-00602-7 (2021).

52 Rehwinkel, J. & Gack, M. U. RIG-I-like receptors: their regulation and roles in RNA sensing. *Nat Rev Immunol* **20**, 537-551, doi:10.1038/s41577-020-0288-3 (2020).

53 Shang, J. *et al.* Quantitative Proteomics Identified TTC4 as a TBK1 Interactor and a Positive Regulator of SeV-Induced Innate Immunity. *Proteomics* **18**, 1700403, doi:https://doi.org/10.1002/pmic.201700403 (2018).

54 Vogel, O. A. *et al.* The p150 Isoform of ADAR1 Blocks Sustained RLR signaling and Apoptosis during Influenza Virus Infection. *Plos Pathog* **16**, e1008842, doi:10.1371/journal.ppat.1008842 (2020).

55 Lei, Y. *et al.* The mitochondrial proteins NLRX1 and TUFM form a complex that regulates type I interferon and autophagy. *Immunity* **36**, 933-946, doi:10.1016/j.immuni.2012.03.025 (2012).

56 Xu, Y. *et al.* Multiplexed Photo-Cross-Linking Reveals Comprehensive Midnolin Interactome: Insights into Ubiquitin-Independent Degradation and Functional Diversity. *J Am Chem Soc* **148**, 11962-11973, doi:10.1021/jacs.5c22099 (2026).

57 Coassolo, S. *et al.* Template-driven scaffolding of SCF(FBXO42) regulates PP2A degradation. *Nature*, doi:10.1038/s41586-026-10368-z (2026).

58 Muhar, M. F. *et al.* C-terminal amides mark proteins for degradation via SCF-FBXO31. *Nature* **638**, 519-527, doi:10.1038/s41586-024-08475-w (2025).

59 Zhang, C. *et al.* Harnessing FBXO31 with Terminal Amide-Functionalized Molecules for Targeted Protein Degradation. *J Am Chem Soc* **148**, 15391-15396, doi:10.1021/jacs.6c02580 (2026).

60 Chung, H. *et al.* Human ADAR1 Prevents Endogenous RNA from Triggering Translational Shutdown. *Cell* **172**, 811-824.e814, doi:10.1016/j.cell.2017.12.038 (2018).

61 Shiromoto, Y., Sakurai, M., Minakuchi, M., Ariyoshi, K. & Nishikura, K. ADAR1 RNA editing enzyme regulates R-loop formation and genome stability at telomeres in cancer cells. *Nature Communications* **12**, 1654, doi:10.1038/s41467-021-21921-x (2021).

62 Karki, R. & Kanneganti, T. D. ADAR1 and ZBP1 in innate immunity, cell death, and disease. *Trends Immunol* **44**, 201-216, doi:10.1016/j.it.2023.01.001 (2023).

63 Rice, G. I. *et al.* Mutations in ADAR1 cause Aicardi-Goutieres syndrome associated with a type I interferon signature. *Nat Genet* **44**, 1243-1248, doi:10.1038/ng.2414 (2012).

64 Beveridge, R., Stadlmann, J., Penninger, J. M. & Mechtler, K. A synthetic peptide library for benchmarking crosslinking-mass spectrometry search engines for proteins and protein complexes. *Nature Communications* **11**, 742, doi:10.1038/s41467-020-14608-2 (2020).

65 Matzinger, M. *et al.* Mimicked synthetic ribosomal protein complex for benchmarking crosslinking mass spectrometry workflows. *Nature Communications* **13**, 3975, doi:10.1038/s41467-022-31701-w (2022).

66 Ma, J. *et al.* iProX: an integrated proteome resource. *Nucleic Acids Res* **47**, D1211-D1217, doi:10.1093/nar/gky869 (2019).

Acknowledgements

We thank the mass spectrometry, imaging and sequencing core facility in Shenzhen Bay Laboratory for their assistance in running samples and collecting data. This work was supported by the National Key

Research and Development Plan of China (2024YFA0920000 to M. Zheng), Shenzhen Medical Research Special Fund (B2401004 to G. Li), Guangdong Special Support Plan for Outstanding Young Talents (2023TQ07A238 to G.L.) and Youth Science Fund Program (Category B) of the National Natural Science Foundation of China (No. 22522703 to G. Li).

Author contributions

G.L. conceived the project and supervised the research. X.Z., C.B. and G.L. designed the experiments and analyzed the data. Z.F. and M.G. contributed to experimental design, data analysis and manuscript preparation. M.Z. supervised the immunology-related studies. F.Z. and T.D. assisted with the F-box screening experiments and immunological validation. P.M. developed the blind-searchblind-search algorithm and contributed to mechanistic analysis of PZPC-induced crosslinks. X.Y. wrote the python program for data processing and generated the figures. X.Z. and G.L. wrote the manuscript with input from all authors. All authors reviewed and approved the final manuscript.

Additional information

Competing interests: G.L. and X.Z. are inventors on a patent related to photoactivation-dependent proximity crosslinking methods and applications (patent no. ZL 2022 1 0820043.9). The remaining authors declare no competing interests.